NASA TECHNICAL NOTE

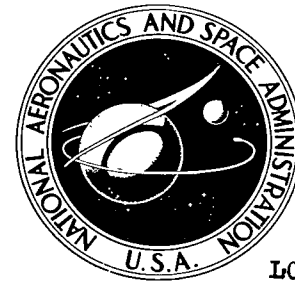

INTERACTION OF INTERMEDIATE ENERGY PROTONS WITH LIGHT NUCLEI

by W. K. Roberts, J. S. Vincent, E. T. Boschitz, K. Gutow, M. Blecher, P. Gugelot, C. F. Perdrisat, L. W. Swenson, and J. R. Priest

Lewis Research Center
Cleveland, Ohio 44135

NATIONAL AERONAUTICS AND SPACE ADMINISTRATION • WASHINGTON, D. C. • AUGUST 1970

1. Report No. NASA TN D-5961	2. Government Accession No.	
4. Title and Subtitle INTERACTION OF INTERMEDIATE ENERGY PROTONS WITH LIGHT NUCLEI		5. Report Date August 1970
		6. Performing Organization Code
7. Author(s) W. K. Roberts, J. S. Vincent, E. T. Boschitz, K. Gutow, M. Blecher, P. Gugelot, C. F. Perdrisat, L. W. Swenson, and J. R. Priest		8. Performing Organization Report No. E-5430
9. Performing Organization Name and Address		10. Work Unit No. 129-02
		11. Contract or Grant No.
12. Sponsoring Agency Name and Address National Aeronautics and Space Administration Washington, D.C. 20546		13. Type of Report and Period Covered Technical Note
		14. Sponsoring Agency Code

15. Supplementary Notes

16. Abstract

The elastic and quasi-elastic scattering of 600-MeV protons from light nuclei has been studied at the NASA Space Radiation Effects Laboratory (SREL) synchrocyclotron. Differential cross sections have been obtained for the scattering of protons from hydrogen, deuterium, helium-3, and helium-4. Polarization was measured for deuterium and ^{4}He nuclei. The p-p cross-section data are in excellent agreement with the predictions from the Livermore phase shifts. Small-angle p-D, p-^{3}He, and p-^{4}He elastic scattering data are compared with calculations based on the multiple scattering theories of Watson and of Glauber. Large-angle p-D data are compared with the predictions of a model recently proposed by Kerman and Kisslinger. Quasi-free p-D scattering differential cross sections at 12° in the laboratory have been measured for nine nuclei between atomic numbers $A = 3$ and $A = 208$ and follow very closely an $A^{1/3}$ dependence.

17. Key Words (Suggested by Author(s))	18. Distribution Statement
Intermediate energy physics Elastic scattering and polarization	Unclassified - unlimited

19. Security Classif. (of this report)	20. Security Classif. (of this page)	21. No. of Pages	22. Price*
Unclassified	Unclassified	57	$3.00

*For sale by the Clearinghouse for Federal Scientific and Technical Information Springfield, Virginia 22151

CONTENTS

INTERACTION OF INTERMEDIATE ENERGY PROTONS WITH LIGHT NUCLEI*

SUMMARY

The differential cross sections and the polarization have been measured for the elastic scattering of 600-MeV protons from the lightest nuclei, hydrogen (H), deuterium (D), helium-3 (^{3}He), and helium-4 (^{4}He). The proton-proton scattering data agree very well with predictions from recently published phase shifts. The p-D, p-^{3}He and p-^{4}He differential cross sections in the forward hemisphere are compared with calculations based on the Glauber approximation in its simplest form. A spin- and isospin-independent nucleon-nucleon scattering amplitude was parameterized as a Gaussian function of momentum transfer in the nuclear center-of-mass system. The nuclear matter distributions for the three nuclei were taken as the product of Gaussian single-particle densities. In spite of these crude assumptions, quantitative agreement was obtained in the region of small momentum transfer. For larger momentum transfer, particularly at the first diffraction minimum in the cross section, theory and experiment deviated considerably. No calculations of the polarization were made. Remler has performed a much more sophisticated calculation on the p-D system by applying Watson's theory in second order with the Livermore phase shifts for the N-N scattering amplitudes and much more realistic wave functions for the deuteron. Remler's predictions of the cross section and of the polarization agree well with the results from this experiment. A preliminary calculation, also based on Watson's multiple-scattering theory, by Ford and Pentz for the p-^{4}He system is in qualitative agreement with both cross-section and polarization data.

The elastic scattering to the backward hemisphere has been studied for the deuteron. An enhanced cross section at large angles was observed which can be explained, in part, by the model recently proposed by Kerman and Kisslinger.

Quasi-free p-D scattering at a deuteron recoil angle of 12° in the laboratory has been investigated for a number of nuclei. The differential production cross section follows very closely an $A^{1/3}$ dependence, which is to be expected from the peripheral nature of quasi-free scattering.

*Contributors to the work compiled in this report were W. K. Roberts and J. S. Vincent, NASA Lewis Research Center; E. T. Boschitz, formerly of the NASA Lewis Research Center and now affiliated with the Institut für Experimentelle Kernphysik, Universität Karlsruhe, Karlsruhe, Germany; K. Gutow and M. Blecher, Virginia Polytechnic Institute, Blacksburg, Va.; P. Gugelot, formerly of the University of Virginia, Charlottesville, Va. and now affiliated with the University of Chicago, Chicago, Ill.; C. F. Perdrisat, College of William and Mary, Williamsburg, Va.; L. W. Swenson, formerly of the College of William and Mary and now affiliated with Oregon State University, Corvallis, Oregon; and J. R. Priest, Miami University, Oxford, Ohio.

INTRODUCTION

During the past few years, there has been an increasing interest in probing the nucleus with intermediate energy particles. This interest is based on the fact that particles for which the wavelength is less than the internucleon spacings may provide information about the nuclear structure which is not forthcoming from experiments at lower energies. Interesting results were obtained by the Brookhaven group at 1 GeV (refs. 1 and 2) on deuterium and helium-4. The data were analyzed by Czyz and Lesniak (ref. 3) and by Bassel and Wilkin (refs. 4 and 5) employing the Glauber diffraction approximation (ref. 6). This approximation gave a rather simple explanation of the ^{4}He data, but did not explain the deuteron data. A number of questions arose, with regard to the following topics: the dependence of the phase of the nucleon-nucleon scattering amplitude on the momentum transfer, the effect of the spin and isospin dependence in the two-body force, reliable determination of the particle nucleon phase from the location and depth of the interference minimum in the particle-nucleus cross section, contributions due to the D-state component in the deuteron, and the range of validity of the Glauber approximation outside the region of small angles and high energies.

Therefore, when the NASA proton synchrocyclotron became operational in 1966, a program was initiated to study the elastic differential cross section and polarization of the lightest nuclei (H, D, ^{3}He, ^{4}He) in the hope of answering some of these questions.

SUMMARY OF EXPERIMENTS

The purpose of the experiments discussed herein was to measure the elastic differential cross section and polarization in p-p, p-D, p-^{3}He, and p-^{4}He scattering. The identification of an elastically scattered proton proved to be a problem because competing multiparticle breakup reactions existed ($p + D \rightarrow p + p + n$, $Q = -2$ MeV; $p + {}^3\text{He} \rightarrow p + p + D$, $Q = -5.5$ MeV; and $p + {}^4\text{He} \rightarrow p + p + {}^3\text{H}$, $Q = -20$ MeV) and because the energy spread of the available beam was 10 and 30 MeV (full width half maximum (FWHM)) for the unpolarized and polarized beams.

In the p-p and p-^{4}He differential-cross-section measurements, elastically scattered protons could be unambiguously separated from inelastic protons by a measurement of their energy. To ensure the elasticity of scattering events in the p-D and p-^{3}He measurements, use was made of the unique relation between the proton scattering angle and the angle of nuclear recoil that exists for an elastic scattering. If the energy of one or both particles is determined and if both particles are detected at the proper angles, the elasticity of the event is assured. This method will be referred to as the associate particle technique.

The particles (proton and/or recoiling target nucleus) were detected in scintillation-counter charged-particle range telescopes. Figure 1 shows the experimental configuration in the proton target area (PTA). Two identical sets of range telescopes were available and could be precisely positioned with respect to a target on a scattering table. A set of telescopes consisted of one seven-element differential range telescope which was generally used to detect protons and define the experimental solid angle, and a two-element telescope which was used to detect the recoiling target nucleus if the associate particle technique was used. Elements 1 and 2 of the seven-element telescope defined the experimental solid angle. A copper energy degrader placed between elements 2 and 3 reduced the incident proton energy to a value such that it would stop somewhere in the array of elements 3 to 7 and a set of four thin copper energy degraders. This allowed the end of the proton range curve to be mapped and was of considerable use in unscrambling elastic and inelastic events. A single seven-element telescope was used in the p-^{4}He differential-cross-section measurement. The other differential-cross-section measurements employed the associate particle technique and a set of telescopes. Despite the fact that the p-p differential cross section could have been determined with only the seven-element telescope, it was found advantageous (because of target composition) to measure it by this method.

The polarization measurements were performed with two appropriate telescope systems.

Throughout these experiments, emphasis was placed on ensuring the elasticity of detected events. In the p-^{4}He differential-cross-section measurement, the differential range curve of protons detected at any angle displayed a Bragg peak which occurred at a range appropriate to the scattering angle. Figure 2 is the differential range curve obtained at a laboratory angle of 15° for p-^{4}He scattering. The mean elastically scattered proton energy was calculated to be 574 MeV. The solid line is the differential curve obtained in a direct beam of 574-MeV protons. The difference between the two curves in the region of 21 to 22 centimeters is due to inelastically scattered protons. A similar distinct separation between elastic and inelastic protons was observed at all angles measured. In the polarization measurements, the separation between elastic and inelastic events was very poor. A calculation or proton yield as a function of thickness of the proton energy degrader showed that only elastically scattered protons penetrated beyond the calculated mean range. Consequently, considerable effort was expended in equalizing the energy degraders in the right and left telescopes and adjusting their value to equal the mean energy proton range.

In those measurements, employing the associate-particle-technique range measurements of one or both particles (scattered proton and recoiling target nucleus) in conjunction with the rotation of one of the telescopes away from the kinematic angle allowed the contamination of observed events by inelastic events to be measured. In all cases, the contamination was less than 10 percent, and corrections to the observed data were made.

The incident beam direction was monitored with a pair of split ion chambers (fig. 1). Beam intensity was monitored by a pair of three-element range telescopes (M_L and M_R) mounted at equal angles to the right and left of the beam line and viewing a monitor target. The monitor rate was calibrated against beam intensity by using an activation technique. An argon ion chamber was used as an auxiliary beam monitor.

Normal and deuterated polyethylene slabs were the targets in the p-p and p-D experiments. Carbon subtraction was performed with matching carbon targets. Gas targets were used in the p-^{3}He determinations and a liquid target in the p-^{4}He determinations.

At 12^o in the laboratory, the p-p and p-D differential cross sections were measured by a magnetic spectrometer and time-of-flight system as one arm of the associate counter telescope system. Elastic events could be unambiguously identified with this system, and the cross sections so obtained agreed well within statistics with the results obtained by using range telescopes.

The time-of-flight system was used to determine the quasi-free p-D production cross section at a deuteron scattering angle $\theta_{D, lab} = 12^o$ for a number of nuclei ranging in atomic number from 3 to 208.

DETAILS OF EXPERIMENT

Beam Development

The experiment was performed at the NASA Space Radiation Effects Laboratory, Newport News, Virginia. The plan view of SREL is shown in figure 3. A beam of 600-MeV protons (nominal energy) was extracted from the cyclotron and focused on the target in the proton target area (PTA) by an array of 21 quadrupole and five bending magnets. The details of the beam transport system are shown in figure 4. Starting from computed values, the magnet settings were manually adjusted to optimize the beam size and the beam divergence at the target position. Fluorescent screens could be inserted in the beam path at beam monitors BM1, BM2, BM3, and BM5 as an aid to beam optimization.

To form a beam with a symmetrically shaped cross section at the target position in the proton target area, it was necessary to insert a copper or lead collimator upstream of the bending magnets (between BM3 and Q16, fig. 4). A 4.5-meter section of vacuum ducting upstream of BM3 was removed for that purpose.

A more detailed study of the beam profile in the proton target area was obtained with split ion chambers (fig. 1). (A split ion chamber is similar to a normal ion chamber except that the collector electrode is split into two equal and independent parts and the ion current is collected from each independently.) The centroid of the beam in a plane perpendicular to the split in the collector electrode was determined by bringing the chamber

to a position in the beam where the current from each half of the chamber was equal. Asymmetries in the split ion chamber system (collector electrode placement, electrometers) were determined by 180° rotation of each split ion chamber about its centerline. The apparent beam centroid shift on split ion chamber rotation was less than 0.5 millimeter for either split ion chamber. Each split ion chamber could be moved remotely in a direction perpendicular to the collector electrode split. Beam profiles were measured by observing the current from one-half of the split ion chamber as it was moved across the beam.

After a beam with an acceptable cross section and divergence at the target position had been obtained by slitting and beam transport system optimization, the split ion chambers 1 and 2, 1 meter upstream and 2.5 meters downstream of the target position, respectively, were positioned so that their centerlines were at the beam centroid. The split ion chambers were then locked in place and provided a reference line to which the main scattering table and monitor table were alined. The estimated uncertainty of the main scattering table alinement was ± 0.05 centimeter and $\pm 0.02^{\circ}$. The sum and difference of the two currents from each split ion chamber were monitored throughout the experiment and displayed on a four-pen strip-chart recorder. A calibration of the difference against the sum of the currents in each chamber as they were moved across the beam was used to estimate the beam misalinement during the experiment. Occasionally, corrections in the settings of bending magnets M6 and M7 were needed to keep the lateral shift of the beam centroids within ± 2 millimeters and the rotation of the beam direction within $\pm 0.03^{\circ}$ of the initial reference line.

Apparatus

A precision scattering table was located 1.5 meters downstream of the beam exit port. The top of the table could be rotated and moved laterally with respect to its base by a small amount to facilitate its alinement with the beam reference line. Four arms pivoted about a post attached to the table. Two arms could be positioned with an accuracy of 0.01° every 0.25° to a maximum of 90° to the right and left of the table centerline. The other two arms could be positioned to $\pm 0.5^{\circ}$.

Scintillation detector telescopes were mounted on these arms. Each scintillator could be positioned to within 0.5 millimeter of the centerline of the arms and with equal precision in its position along the arms.

An auxiliary table positioned 3.5 meters downstream from the main scattering table held a pair of monitor telescopes (M_L and M_R, fig. 1) which monitored the beam intensity. The telescopes were mounted at equal angles ($\sim 35^{\circ}$) to the right and left of the beam centerline and viewed an aluminum target 38 by 38 centimeters and 0.6 centimeter thick. The sum of the counts observed in the two telescopes was essentially independent

of the beam position on the monitor target, while the ratio of the left to right count rate was a sensitive measure of the misalinement of the beam. These telescopes and this target were the primary beam monitor. Such monitoring of the beam intensity was adequate as long as the beam size was smaller than the main target size. During some parts of the experiment, this condition could not be maintained. In these cases, an additional counter telescope, which viewed mainly the experiment target, was mounted above the scattering table at about 45° to the scattering plane.

Counters

Scattered protons and recoiling target nuclei were detected in range telescopes. In the p-p, p-D, and p-He^3 experiment, a coincidence between the scattered proton and the recoiling target nucleus (associate particle) was one of the conditions necessary to ensure the elasticity of the scattering event. Detectors 1 to 7 on one arm and detectors 8 and 9 on the other arm formed one set of associate counter telescopes. In the polarization measurements, two identical sets of associate counter telescopes were used. In the p-^{4}He experiments, the recoiling target nucleus was not detected, therefore only the arms containing detectors 1 to 7 were used.

The telescope consisting of detectors 1 to 7 was normally used as a differential range telescope. A large block of copper was placed between detectors 2 and 3 as the main energy degrader. Thin copper plates were then sandwiched between detectors 3 and 7 to scan the end of the range curve. Detectors 3 to 7 were large enough to keep counting losses due to multiple scattering in the copper degraders smaller than 1 percent.

Each detector in the telescopes consisted of a plastic scintillator, a lucite light guide, and a photomultiplier assembly. The anode output and the dynode chain were connected by means of 50-ohm coaxial cables to a fast discriminator and to a variable high-voltage supply located in the counting room. The scintillators were typically 0.6 centimeter thick and had the following frontal dimensions: detector 1, 0.6 by 7.5 centimeters for the liquid ^{4}He and gaseous ^{3}He targets and 2.5 by 7.5 centimeters for solid targets; detector 2, 1.2 by 5.1 centimeters; detectors 3 to 9, 12.5 by 17.5 centimeters. On occasion, detector 8 was reduced to 0.5 millimeter in thickness. Detectors 2 to 7 and detectors 8 and 9 were mounted so as to be movable as units. Detector 1, the detector block holding detectors 2 to 7, and the detector block holding detectors 8 and 9 could be positioned independently to optimize the angular resolution, solid angle, and random coincidence rates.

In the case of a liquid ^{4}He or gaseous ^{3}He target, scintillators 1 and 2 defined the target volume and the solid angle. In the case of solid targets, scintillator 1 was chosen to be slightly larger than scintillator 2, the solid-angle-defining scintillator. The presence of scintillator 1 in this condition helped reduce the number of random events.

Electronics

Figure 5 is a block diagram of the electronics. The scintillator, light pipe, photomultiplier tube, high-voltage supply, and discriminator combinations are shown simply as detectors, and not all delays necessary for prompt timing are shown. The coincidence circuits are basically "and" gates. The electronics consisted of two parts, the logic for the solid-angle-defining telescope and the logic for the associate telescope. In the defining telescope, two- to sevenfold coincidences are formed multiplicatively. Only the two- and threefold random coincidences shown were normally measured. The removal of random coincidence events is discussed in appendix A.

In the associate telescope, a double coincidence ($8 \cdot 9 = S$, where S is the associated counter symbol) was formed. Occasionally, the range of the recoiling target nucleus was too small to reach detector 9; in those cases, 9 was removed from the coincidence. Whenever needed, the coincidence between both telescopes was formed electronically with "strobed coincident units." A strobed coincident unit is a set of coincidence circuits in which one input signal of each coincidence is a common logic signal (the strobe signal). In the present setup, the strobe signal is provided by the associate telescope. The individual strobed coincidences are labeled $III \cdot S$, $IV \cdot S$, etc. The chance rates between the two telescopes, labeled $III \cdot (S)$, $IV \cdot (S)$, etc., were determined in a second strobed coincidence unit by delaying the strobe signal by 58 nanoseconds, which is approximately the time taken by the coasting circulating cyclotron beam to make one revolution in the cyclotron. Single events and coincident events of interest were accumulated on scalers.

The electronics (discriminators, coincidence circuits, scalers) employed in the experiment was capable of operation at a 100-megahertz synchronous rate.

Beam Characteristics

During the course of these experiments, two methods of beam extraction were used. The differential cross section and the polarization of ^4He were measured by using normal beam extraction methods. In the other experiments, stochastic extraction became available. With normal extraction, a maximum beam intensity on target of 2×10^{11} protons per second could be attained, but only 2×10^7 protons per second could be tolerated without unduly larger telescope chance coincidence rates. (At 2×10^7 protons/sec, a maximum chance rate of 20 percent was observed.) With stochastic extraction a maximum beam intensity on target of 10^{11} protons per second was attained.

With normal extraction the beam is modulated on both a macro- and micro-time scale, as shown in figure 6. Macrobursts of particles of time duration $T = 30$ to 100 microseconds are produced at a frequency of $F \approx 54$ hertz. Within the macroburst,

microbursts of particles of time duration $t \approx 6$ nanoseconds occur at a frequency $f \approx 17.5$ megahertz, leading to a duty cycle of FTft = 2×10^{-4} to 6×10^{-4}. In general, the intensity of both the macro- and microbursts has a time structure. The intensity of the macrobursts has a roughly isosceles triangular modulation. No attempt was made to analyze the time structure of the microbursts.

With stochastic extraction, 90 to 95 percent of the beam was spilled from the cyclotron with the same time structure as shown in figure 6, with the remaining 5 to 10 percent uniformly extracted during the time between macrobursts. To utilize the good-duty-cycle portion of the beam, the electronics were gated off during a 1-millisecond period symmetrically located with respect to the beginning of each macroburst. Maximum gated beam intensities of 5×10^9 protons per second could be obtained with random rates of less than 10 percent of observed rates. In general, the beam intensity used with stochastic extraction was kept low enough that random rates were less than or equal to 2 percent of the observed rates.

Polarized protons were produced by scattering the internal proton beam from a carbon target mounted inside the cyclotron at an azimuthal position such that some of the protons scattered at $9^\circ\pm1^\circ$ entered the beam transport system. The maximum polarized proton beam intensity on target was about 3×10^7 protons per second, and the time structure was the same as with the unpolarized beam. The polarization of the beam was determined in separate experiments by scattering from carbon at 6°, 8°, and 10° and from hydrogen at 15° in the laboratory system. Asymmetries of 0.119 ± 0.002, 0.146 ± 0.002, and 0.148 ± 0.003 at 6°, 8°, and 10°, respectively, for p-^{12}C and of 0.195 ± 0.017 for 15° p-p scattering were measured. Analyzing powers of 0.325 ± 0.015 at 6°, 0.384 ± 0.015 at 8°, and 0.410 ± 0.015 at 10° for p-^{12}C, and of 0.488 ± 0.025 at 15° for p-p scattering, were obtained by interpolating the experimental values of references 7 and 8 to the appropriate proton energy. The data in references 7 and 8 cover an energy range from 310 to 700 MeV and have absolute uncertainties of ±3 percent. The beam polarization calculated from the measured asymmetries and these analyzing powers was 0.369 ± 0.015 using p-^{12}C data and 0.400 ± 0.040 using p-p data.

Monitor Calibration

The primary monitor (M_L, M_R) was calibrated by activation of either carbon or polyethlene foils through the reaction $^{12}C(p,pn)^{11}C$, $\sigma_{act} = 30.5\pm0.6$ millibarns (ref. 9). The cyclotron beam was allowed to strike the activation foil for 10 minutes, and the number of primary monitor counts was recorded. Subsequent comparison of the foil annihilation gamma-ray activity with a calibrated ^{22}Na source allowed a flux calibration (incident proton/monitor count) to be determined. In general, flux calibrations were good to ±6 percent.

Beam Energy and Calibration

The proton beam energy was determined by scattering protons from carbon and hydrogen (CH_2) and by measuring their mean range in a counter telescope. After correcting for the target thickness and the kinematic energy loss at the angle measured, a mean range in copper was found which corresponded to 594±2 and 554±2 MeV for the unpolarized and polarized proton beams, respectively. Stochastic extraction caused a slight reduction in energy, namely 580 and 544 MeV, respectively. The energy spread (FWHM) was deduced from the shapes of the range curves and amounted to 10 and 30 MeV for the unpolarized and polarized beam for both methods of beam extraction.

Since the beam handling system was designed to be achromatic and also intended to be fixed in geometry, it was impossible to improve the energy resolution of the extracted beam.

Range Telescope Detection Efficiency

One of the basic problems in using range telescopes for the detection of high-energy protons is the determination of detection efficiency. Telescope detection efficiency for a given thickness of energy degrader is defined as the number of protons and proton-produced reaction products detected in the telescope after passage through the energy degraded divided by the incident number of protons.

In determining the yield of the scattered protons in the cross-section measurements, detection efficiency for different energy degraders in the telescope had to be known. Therefore, a plot of detection efficiency as a function of proton energy and reduced range was generated (fig. 7). Reduced range is defined as the equivalent amount of copper in the beam divided by the mean range of protons in copper. The relative error in the detection efficiency for reduced ranges greater than 95 percent is of the order of ±10 percent and approaches zero as the reduced range approaches zero. Figure 7 has been constructed from range curves measured at five proton energies. At three energies, the telescope was placed in the direct proton beam, at two other energies it was placed in a beam of scattered protons.

The various energies of the direct proton beam were obtained by degrading the 600-MeV beam with absorbers placed in the break of the vacuum duct of the beam transport system (between BM3 and Q16, fig. 4). The range curves were obtained by inserting a variable copper wedge between detectors 2 and 3 of the telescope. Copper energy degraders 0.625 centimeter thick were placed between detectors 3, 4; 4, 5; 5, 6; and 6, 7. With this arrangement, five range curves were obtained for each incident proton energy, each curve separated by 0.735 centimeter equivalent copper thickness (absorber and scintillator). The comparison of the five different range curves checked the system in

regard to counter efficiency and random coincidence rate. The telescope efficiency was found to be greater than or equal to 98 percent, and it was observed that the coincidence rate in 1·2·3 contained a beam-level-dependent random rate which could not be removed by a simple delayed coincidence method. With stochastic extraction, sufficient usable beam was available so that the beam level could be reduced to a point where random coincidences ceased to be a problem. However, with normal beam extraction, beam intensities of less than 10^7 protons per second were too costly of beam time. Consequently, random subtractions were handled, as outlined in appendix A.

Figure 8 shows a range curve obtained at a proton energy of 574 MeV. The gradual decrease in the number of protons with increasing energy degrader is due to the removal of protons by reactions. Range curves were also measured at 493, 477, 412, and 288 MeV.

A Monte Carlo calculation for the penetration of the protons through a copper slab was performed (private communication from P. C. Gugelot, University of Chicago). Known reaction cross sections in the energy range 10 to 600 MeV and different reasonable assumptions for the angular distribution and energy spectra of the reaction products were used. The Monte Carlo calculations agreed to within 10 percent with the experimentally observed absorption curve.

Targets

The hydrogen targets used in the p-p scattering measurements were thin polyethylene sheets 5.1 by 5.1 centimeters and ranging in thickness from 0.025 to 1.28 centimeters. The targets were weighed and the frontal areas of each carefully measured. The thickness of each foil was also measured; the deviations from a constant thickness varied from ±5 percent for the thinnest foil to ±0.6 percent for the thickest foils. Average areal densities for each foil were calculated on the basis of its mass and frontal area. An error in areal density was assigned to each on the basis of the linear sum of the error in frontal area and average thickness.

To perform the necessary carbon subtractions, a set of precisely machined carbon foils were prepared from high-density carbon. The areal densities were again computed on the basis of mass and frontal area. The variations in thickness were very small ($<\pm 0.001$ cm) for each foil. It was found that the average density varied for each foil. Because they were cut from the same block of carbon, it was assumed that a microscopic variation of density occurred throughout the foils. Consequently, an error of ±3 percent was assigned to each calculated areal density.

The deuterium targets were deuterated polyethylene. The deuterium to deuterium-plus-hydrogen content was greater than or equal to 98 percent of total hydrogen for all targets analyzed. Because the foils were uneven at their edges, the average density was

determined by Archimedes' principle and $\rho_{CD_2} = 1.067 \pm 0.003$ grams per cubic centimeters was found. The areal densities were calculated on the basis of average foil thickness. Carbon subtractions were obtained using the carbon foils previously mentioned.

The ^{3}He targets consisted of gaseous ^{3}He contained in vessels 15 centimeters in diameter. For very forward angles, the target walls were 0.0025 centimeter thick Havar foil, and the target was filled with ^{3}He to an absolute gas pressure of 3 atmospheres. For larger angles, the wall thickness was increased to 0.0075 centimeter and gas pressure to 11 atmospheres. The wall thickness limited the forward angles which could be measured because the recoiling ^{3}He particle had to be detected.

The liquid ^{4}He target was loaned to us from the Brookhaven National Laboratory. The target chamber was a cylindrical container 12.5 centimeters high and 10 centimeters in diameter constructed of 150 layers of 0.0025-centimeter-thick super insulation (aluminum-coated mylar) connected to a 25-liter liquid-helium reservoir. For background measurement, the liquid in the target volume could be returned to the reservoir. The density of residual gas in the empty target state was accounted for in the background subtraction.

Magnetic Spectrometer and Time-of-Flight System

The p-p and p-D cross sections were measured at 12° in the laboratory using magnetic deflection and time of flight. With the same system, the quasi-elastic p-D cross section was measured for a number of nuclei between atomic numbers 3 and 208. Figure 9 shows the experimental arrangement. The associate particle coincidence technique was used in the cross-section measurements. Figure 10 is a block diagram of the electronics employed. The associate detector signal is defined as S. Detectors C1, C2, C3, and C4 constitute the time-of-flight telescope. Time of flight was measured from detector C1 to detector C3 (separation, 700 cm). Detector C2 was the defining detector and had dimensions of 5.08 by 1.27 by 0.6 centimeters. Detector C3 had dimensions of 33 by 12.7 by 0.6 centimeters and could be rotated to decrease the momentum bite of the system. Detectors C1 and C4 had dimensions of 7.64 by 2.54 by 0.6 and 38.2 by 17.75 by 0.6 centimeters, respectively. The bending magnet field was monitored by a calibrated hall probe. In the p-D quasi-elastic measurements, the associate detector signal S was switched out of the logic.

Initial timing of the time-of-flight circuitry was accomplished by employing p-D scattering. The proton was detected in the associate arm and the deuterons in the time-of-flight telescope. The scattered deuterons were chosen to make the alinement because their momentum per unit charge had the largest value of any particle which would be de-

tected. This allowed unambiguous identification of deuterons during the initial alinement. Initial delays (not shown in fig. 10) between each detector element was adjusted visually on an oscilloscope to bring the logic signals from each element in time coincidence. A calculation made previous to the alinement indicated the relative timing delays between all detectors which could be expected over the range of momentum and nuclear charge to be investigated. The logic pulse widths of S, C2, and C4 and logic S·C2·C1 were preadjusted to the values shown. The widths chosen were at least two times the calculated values. After the initial alinement with forward scattered deuterons, logic pulse C1 was delayed by 15 nanoseconds. This ensured that logic pulse C1 was always overlapped by logic pulses S and C2 in all subsequent situations and that logic pulse S·C2·C1, the stop signal, was well timed with respect to C1. Logic signal C3 was delayed by $\tau 2$ = 5 nanoseconds, ensuring that C3·C4 was in time with only C3; τ^3 was then set to 30 nanoseconds, which ensured that the start signal S·C2·C1·C3·C4 was well timed with respect to C3. Signal S·C2·C1 was delayed one microburst period (~58 nsec) and the coincidence rate with C3·C4 was measured to determine the chance start rate. The chance start rate was always less than 1 percent of the observed start rate.

DATA ACCUMULATION

The main purpose of the experiment was the measurement of the elastic differential cross section and polarization in p-p, p-D, p-^{3}He, and p-^{4}He scattering. In p-^{4}He scattering, where the first excited state is 20 MeV above the ground state, a sufficient condition for the identification of elastically scattered protons could be based on the proton range. In p-p, p-D, and p-^{3}He scattering, the energy spread of the unpolarized and polarized beams was much larger than the energy needed to break up the target nuclei. Consequently, a measurement of the scattered proton energy on the basis of its range was insufficient to ensure the elasticity of the scattering event. To surmount this difficulty, the associate counter technique was employed. The associate counter technique relies on the unique kinematic relation that exists between the angle through which a proton is scattered and the angle at which the elastically recoiling target nucleus is ejected. A coincidence between the scattered proton in one telescope and the recoiling nucleus in a second telescope set at the proper angle, coupled with a range requirement for either or both the proton and recoiling target nucleus, uniquely identifies an elastic event. The range requirement was necessary to eliminate coincidences at the conjugate angles caused by the multiparticle breakup reactions, that is, $p + p \rightarrow \pi + D$, $p + D \rightarrow p + p + n$, $p + {}^3He \rightarrow p + p + d$. A second method of uniquely identifying the elastically recoiling target nucleus employed a magnetic spectrometer and time-of-flight system as one arm of the associate counter telescopes. This method was employed at only one angle (12^o in the laboratory) and was used to check the differential p-p and p-D cross

sections obtained by the first method.

The proton-proton differential cross section was measured by using the associate particle method without additional particle identification. Only one set of telescopes was used. The yield was obtained as the difference between a measurement with a polyethylene foil and one with a carbon foil. The cross section at 90° in the center of mass was also measured with a hydrogen gas target of 65 atmospheres pressure. The cross section obtained agreed within statistics with the 90° data point obtained with the solid target. As an additional check, the proton cross section at 12° in the laboratory system was determined by using a magnetic spectrometer and time-of-flight system. Good agreement with previous data was obtained. The differential cross section $(d\sigma/d\Omega)_{cm}$ is 5.45 ± 0.16 millibarns per steradian for the telescope method as compared to 5.78 ± 0.21 millibarns per steradian for the time-of-flight method.

For proton-deuteron scattering, the differential cross section and the polarization were measured similarly to the p-p scattering except that the breakup of the deuteron yielded nonelastic coincident events, which necessitated the identification of at least one of the particles.

For the forward hemisphere (laboratory scattering angle, $\theta_{lab} \leq 60^{\circ}$), a range requirement was placed on both the scattered proton and the recoiling deuteron. The yield was obtained from the difference between the CD_2 and carbon measurements, each of which was taken both without a deuteron absorber and then with sufficient absorber to stop recoiling deuterons.

Proof that breakup events were effectively being eliminated was obtained at a number of proton angles by measurement of the coincidence rate when the associate telescope was rotated away from the kinematically correct angle. Figure 11 is the coincidence rate as a function of deuteron detector angle for a proton scattering angle of 60° in the laboratory system. In all cases, the coincidence rate was reduced to less than 2 percent of the rate at the kinematically correct angle after rotations corresponding to slightly more than one-half the angular width of the associate telescope.

For proton angles larger than 60° (lab), the solid-angle-defining telescope was used to detect the deuterons, and the protons were detected in the associate telescope. A range requirement was imposed on only the protons since the detection efficiency of a range telescope for high-energy deuterons is small and not well known.

At several angles, the range curves for the scattered proton were measured in detail (fig. 12). From the shape of these curves, the contribution of nonelastic events could be estimated. Subsequent data were taken with the usual carbon background subtraction $N_{CD_2} - N_C$, where N_{CD_2} and N_C are obtained from pairs of runs with absorbers that bracket the end of the proton range curve. The contribution from inelastic events was estimated from curves similar to that shown in figure 12, and corrections were applied to the observed coincidence rate. The fraction of observed coincidences

caused by inelastic events was also measured by moving the associate counter off the kinematic angle, and agreed with estimates obtained from the proton range curves.

As an additional test, the magnetic spectrometer and time-of-flight system was used to separate deuterons from breakup protons. The cross section was measured at $\theta_{p, lab} = 12^{o}$ and $\theta_{D, lab} = 12^{o}$ ($\theta_{p, lab} = 127^{o}$), and the values found agreed very well with the cross section determined by the coincidence-range method.

For the polarization measurement, all four telescopes shown in figure 1 were used. During the experiment, the telescope pairs were interchanged a number of times for each angle to eliminate some of the instrumental asymmetries.

To ensure target symmetry during the polarization measurements, the targets were mounted parallel to the beam line. Because a carbon subtraction was necessary and because a large fraction of the beam did not strike the target, a monitor which viewed the target and was mounted above the scattering table was employed.

The p-^{3}He differential cross section was measured in a fashion identical to the forward angle p-D data, with the exception that only protons and ^{3}He particles which stopped within the full width of their respective differential Bragg peaks contributed coincident events. As in the case of p-D scattering, nonelastic events caused by the breakup of the target nucleus could add false events to the true data. In order to investigate this contribution, the proton and ^{3}He absorption curves were mapped. From their shape, it was apparent that nonelastic events did not significantly contribute to the coincidence rate, if the range requirements mentioned previously were imposed.

The p-^{4}He cross section and polarization were measured with the seven-element range telescopes only. For the polarization measurement, two matched range telescopes, positioned at equal angles left and right, recorded protons scattered from the liquid ^{4}He target. Because the energy resolution of the incident polarized proton beam was 30 MeV (FWHM), elastic and inelastic events could not be unambiguously separated. Asymmetries were calculated for protons which stopped in the various range increments between detectors 3 and 7 (3, 4; 4, 5; 5, 6; 6, 7). By systematically adjusting the main absorber as a function of scattering angle, the front of detector 5 was kept at the expected mean range of the elastically scattered proton based on the mean incident beam energy. Consistent results were obtained using increments (5, 6 and 6, 7). These data were used to calculate the polarization. Increments 3, 4 and 4, 5 were generally either higher or lower and were probably contaminated with inelastic scattering events.

DATA REDUCTION

Differential Cross Section

The differential cross section was computed from the following formula:

$$\frac{d\sigma}{d\Omega} = \frac{N}{\varphi G(\theta)\epsilon\rho}$$

where

N	number of elastically scattered protons detected
φ	number of incident protons
$G(\theta)$	geometry factor
ϵ	efficiency of detecting protons
ρ	nuclear density of target

For liquid and gas targets,

$$G(\theta) = \frac{x_1 x_2 h_2}{L(L - l)\sin\theta}$$

where

x_1	width of first detector scintillator in a telescope
x_2, h_2	width and height of second detector scintillator
L	distance from target to second detector
l	distance between first and second detector
θ	laboratory scattering angle

For solid targets,

$$G(\theta) = \frac{x_2 h_2 t}{L^2}$$

where t is the target thickness parallel to beam, and all other variables have been defined.

Polarization

The asymmetry calculated in a polarization experiment is the product of the incident beam polarization P_1 and the polarization of the target P_2:

$$\mathscr{A} = P_1 P_2$$

Asymmetry is defined as the ratio of the number of incident particles scattered right minus the number scattered left divided by the sum. If the number scattered right and detected by detector a is N_{Ra} and the number scattered left and detected by detector b is N_{Lb}, the asymmetry is

$$\mathcal{A}_a = \frac{N_{Ra} - N_{Lb}}{N_{Ra} + N_{Lb}}$$

If the detectors are switched so that now detector a is on the left and detector b is on the right, the asymmetry is

$$\mathcal{A}_b = \frac{N_{Rb} - N_{La}}{N_{Rb} + N_{La}}$$

The asymmetry computed was the average of measurements made in these two configurations.

The false asymmetry due to beam misalinement was estimated from the following:

$$\delta\mathcal{A} = \frac{d^2\sigma}{d\Omega\, d\theta} \frac{\Delta\theta}{\frac{d\sigma}{d\Omega}}$$

where $d^2\sigma/d\Omega\, d\theta$ is the slope of the differential cross section and $\Delta\theta$ is the accumulated, estimated alinement errors.

The maximum estimated value of false asymmetry is ±0.03 and ±0.045 for the p-D and p-^{4}He measurements, respectively.

RESULTS OF EXPERIMENTS

The differential cross section and polarization data for p-p, p-D, p-^{3}He, and p-^{4}He scattering are listed in tables I to VI and plotted in figures 13 to 16 as a function of center-of-mass angle. The p-p data agree very well with the predictions from recently published phase shifts from Livermore (ref. 10). The p-^{4}He data (fig. 16) show an interesting feature. There is a diffraction pattern in both the cross section and the polarization near 35°. The p-^{3}He cross section (fig. 15), in contrast, displays no pronounced minimum but only a shallow minimum. In the p-D cross section (fig. 14), even this minimum has disappeared and just an inflection in the cross section at 55° is present. Besides these differences in the forward hemisphere, there is a considerable backward

peaking of the p-D cross section near 180°. This has been observed earlier in experiments at 1 and 1.5 GeV (refs. 2 and 11). The p-D polarization pattern is quite different from that for ^{4}He. There is no large polarization at large angles as in the p-^{4}He case.

ERROR DISCUSSION

Absolute and relative errors have been assigned to each cross-section data point. The main sources of the absolute error are monitor rate against incident proton flux calibration and uncertainty in the solid angle defined by the telescope. The main sources of relative error are the error in the scattered particle rate after suitable random and background rate subtraction and the estimated error in telescope efficiency. Additional sources of relative errors are the target areal density, and in the case of solid targets the error in the orientation of the target with respect to the beam line. Targets were oriented to $\pm 1^{\circ}$. With the solid targets a fraction of the beam missed the target. Comparison of vertical and horizontal monitor rates with targets of various sizes showed that up to 2 percent of the beam passed above or below a 5- by 3.5-centimeter target. It was assumed that 99 ± 1 percent of the beam struck the solid targets at all times, leading to a 1 percent absolute error. A small beam intensity dependence of scattered rate was observed in the p-p cross-section determination. The observed scattering rate was between 0.6 and 1.2 percent lower than it should have been based on an extrapolation of rate against beam intensity to very small beam intensities. A correction was applied.

In the polarization measurements the predominant source of relative error was the statistical error in the right-left count rates after suitable background and random rate subtraction.

In table VII the various sources of error have been tabulated for the various cross-section determinations. The upper and lower limits of the errors encountered have been noted. The total absolute error in each cross-section determination is also shown and is computed as the quadratic sum of the various absolute errors. The relative errors were different for each angle in any determination and have been weighted inversely as the relative error if more than one measurement was made at an angle. The relative errors in the cross-section and polarization determinations are shown in figures 13 to 16.

THEORY

After some unsuccessful attempts to interpret the p-^{4}He cross section at 1 GeV in terms of the strong absorption model or the optical model (ref. 1), Czyz and Lesniak (ref. 3) and Bassel and Wilkin (refs. 4 and 5) applied the Glauber diffraction approximation (ref. 6) to this problem. This approximation is not at all new. It has been applied

many times to the deduction of neutron cross sections from measurements made on the deuteron. What is new is that this approximation gave a rather simple and transparent explanation of the Brookhaven differential-cross-section data. Since this approximation applies also to this data, a brief description of the Glauber formalism as applied by Czyz and Lesniak follows.

In this approximation the differential cross section for purely elastic scattering is given by

$$\frac{d\sigma}{d\Omega} = \left| \langle \psi_o | F | \psi_o \rangle \right|^2 \tag{1}$$

where F is the nucleon-nucleus scattering amplitude and ψ_o is the ground-state wave function of the target nucleus.

$$F = \frac{ik}{2\pi} \int d^2b e^{i\vec{q}\cdot\vec{b}} \left[1 - e^{iX(\vec{b})} \right] \tag{2}$$

where k is the incident momentum, q the momentum transfer, $\vec{b}$ the impact parameter, $X(\vec{b})$ the phase shift function, and

$$\Gamma(b) = \left[1 - e^{iX(\vec{b})} \right]$$

is the profile function. The Glauber approximation is based on two assumptions:

(1) The proton-nucleus phase shift is the sum of the proton-nucleon phase shifts

$$X(\vec{b}) = \sum_{j=1}^{a} X_j(\vec{b}) - \vec{s}_j \tag{3}$$

for a nucleons in the nucleus, $\vec{s}_j$ being their position vectors. It follows that

$$\Gamma(\vec{b}, \vec{s}_1, \ldots, \vec{s}_a) = 1 - e^{iX(\vec{b}, \vec{s}_1, \ldots, \vec{s}_a)}$$

$$= 1 - \prod_{j=1}^{a} \left[1 - \Gamma_j(\vec{b} - \vec{s}_j) \right]$$

$$= \sum_j \Gamma_j(\vec{b} - \vec{s}_j) - \sum_{j<m} \Gamma_j(\vec{b} - \vec{s}_j)\Gamma_m(\vec{b} - \vec{s}_m) + \sum \Gamma\Gamma\Gamma \ldots \tag{4}$$

This expansion is very important in the multiple-scattering theory. The first term corresponds to single scattering, the next to double scattering, the next to triple scattering, etc. The negative sign of the double-scattering term, causes a destructive interference between single and double scattering.

(2) If it is assumed that the Fermi motion of the nucleus is small with respect to the incident momentum k, the nucleons can be considered as being fixed in their positions. The observed proton-nucleus amplitude is F averaged over the positions of the nucleons in the nucleus

$$F_{fi}(q) = \langle f | F | i \rangle$$

In order to evaluate this matrix element, it is necessary to know the individual profile functions $\Gamma_j(\vec{b} - \vec{s}_j)$. If the incident particles j^{th} target nucleon scattering amplitude is known,

$$f_j(q) = \frac{ik}{2\pi} \int d^2b e^{i\vec{q}\cdot\vec{b}} \Gamma_j(b) \tag{5}$$

then the profile function can be constructed by the inverse transformation

$$\Gamma_j(b) = \frac{1}{2\pi ik} \int d^2q e^{-i\vec{q}\cdot\vec{b}} f_j(\vec{q}) \tag{6}$$

With this, the following equation is obtained:

$$F_{fi} = \Theta \int d^3\vec{r}_1, \ldots, d^3\vec{r}_A \left| \psi(\vec{r}_1, \ldots, \vec{r}_A) \right|^2$$

$$\times \frac{ik}{2\pi} \int d^2b e^{i\vec{q}\cdot\vec{b}} \left\{ 1 - \prod_{j=1}^{A} \left[1 - \frac{1}{2\pi ik} d^2q e^{-i\vec{q}\cdot(\vec{b}-\vec{s}_j)} f_j(q) \right] \right\} \tag{7}$$

where Θ is a factor correcting for the recoil. The proton-nucleus cross section can be calculated if the wave function and the scattering amplitude of the incident particle and the individual protons and neutrons of the target nucleus are known. In their first calculation, Czyz and Lesniak (ref. 3) assumed that the nucleons in ^{4}He are independent of one another, and therefore they used a simple product of Gaussians for the ^{4}He particle wave function

$$|\psi_o|^2 = \prod_{j=1}^{A} \rho_o e^{-r_j^2/R^2} \tag{8}$$

where R is the rms radius of the distribution of point nucleons in the target and is computed from electron scattering data.

Neglecting spin and isospin dependence, Czyz and Lesniak assumed a parametized form for the nucleon-nucleon scattering amplitude which fits the cross-section data fairly well

$$f_i(\vec{k}, \vec{q}) = \frac{i + \alpha_i}{4\pi} k\sigma_{T,i} e^{-1/2(aq^2)} \tag{9}$$

where $\sigma_{T,i}$ is the total nucleon-nucleon cross section, α_i the ratio of real to imaginary part of the nucleon-nucleon scattering amplitude, and a the slope of the nucleon-nucleon cross section.

In the past 2 years, the Glauber formalism has proven to be very successful, being applied to many high-energy problems like hadron-hadron scattering, meson production, etc. (refs. 12 to 16).

There has been some concern about the limitations of the Glauber approximation. It is a high-energy, small-angle approximation. Yet the physically most interesting part of the cross section is not located at small angles, but is in the interference region or at even larger angles. From a study of the dip, for instance, information can be extracted about the phase of the particle-nucleon amplitude at nonzero angles, and the region of larger momentum transfer might reveal interesting details about the nuclear wave function. All this is possible only if we can rely on the basic scattering theory. Recently, efforts have been made by Schiff (ref. 17) and Ross (ref. 18) to modify Glauber's theory to extend its range of validity to larger angles. Since Glauber's theory can be derived from Watson's multiple-scattering theory (ref. 19) by suitably approximating the propagator, such attempts to incorporate large-angle corrections may be viewed alternately as attempts to approximate the propagator more accurately. Pumplin (ref. 20) and Remler (ref. 21) have stressed the importance of a careful treatment of the propagator. Studying the behavior of the integrands in the multiple-scattering integrals, Ford and Pentz (ref. 22) have proposed a new approximation based on Watson's multiple-scattering formalism. To evaluate the error in the various approximations (those of Schiff, Glauber, and Ford and Pentz), the approximate double-scattering terms are compared with the exact Watson theory results. Ford and Pentz show that their suggested approximation predicts the correct phase and magnitude of the double-scattering term within 5 percent for scattering angles between 0° and 80° center of mass. They also show that the Glauber approximation gives fairly good values for the magnitude of this term but fails to predict the proper phase at larger angles.

DISCUSSION AND CONCLUSIONS

Differential Cross Section and Polarization

The present data have been analyzed in terms of the Glauber theory following Czyz and Lesniak's simplified calculation. The experimental and calculated differential cross sections for ^{4}He are shown in figure 17. The curves for the calculated differential cross sections are labeled to indicate the number of multiple-scattering terms included in each calculation (one to four).

For small momentum transfer, where the theory is most reliable, the agreement with the data is good. The absolute magnitude, the slope, and the location of the minimum are well reproduced. Beyond the minimum the calculation underestimates the differential cross section. Observing that the most recent Stanford data (ref. 23) indicate the need of spreading out the charge density of the ^{4}He particle, Bassel and Wilkins (refs. 4 and 5) used modified wave functions which produced better fits to the p-^{4}He cross section at larger angles. Unfortunately, it was found that little can be learned in regard to the correlations between the individual nucleons.

The results for p-^{3}He scattering are presented in figure 18. The same product wave function for ^{3}He with a radius corresponding to the rms radius obtained from electron scattering was used. This theoretical curve overestimates the cross section at the secondary maximum, which might be due to the fact that in the Gaussian model the high momentum components of the wave function are overestimated in the case of ^{4}He but underestimated for ^{3}He. The use of a better ^{3}He wave function will probably produce better agreement.

An interesting result is seen in figure 19. The p-D calculation produces a pronounced dip in the cross section which does not exist in the data. The absence of a minimum in the p-D angular distribution presented a puzzle for quite a while. The immediate idea that came to mind was to assume a momentum dependence of the phase of the nucleon-nucleon scattering amplitude (ref. 2). In the absence of a fundamental theory of the nucleon-nucleon interaction, there is no way of predicting such a phase factor. Furthermore, the phase at nonzero angle is precisely what cannot be measured in an ordinary p-p cross-section measurement. On the other hand, the interference between single and double scattering is very sensitive to the phase. A calculation by Glauber (ref. 24) showed that when the phase variation which would be required to fit the p-d cross section is used, the minimum in the p-^{4}He data disappears also.

The next suggestion made by Czyz (ref. 25) and others was the spin dependence in the two-body force. The most general form of the spin-dependent scattering amplitude includes five terms, three of them bilinear in spin. Those terms that are bilinear in the spins will contribute nothing to the single-scattering amplitude in ^{4}He, since the nucleon

spins are paired in ^{4}He. They will, on the other hand, give strong contributions in the deuteron. In proton-deuteron scattering (spin $1/2^+$ particle scattered from a spin 1^+ particle), there are 11 spin-dependent amplitudes, and there is a good chance that a number of terms which contribute incoherently will tend to fill in the minimum. A calculation by Franco (ref. 26) and a similar one by Kujawski, Sachs, and Trefil (ref. 27) show that the inclusion of the spin dependence in the two-body interaction is a step in the right direction, but do not fully explain the p-D data. Unfortunately, there are no polarization data at 1 GeV that would allow even the qualitative features of these calculations to be tested.

Finally, an explanation of the p-D and π-d cross sections was given by Harrington (ref. 28) and by Coleman and Rhoades (ref. 29). It was shown by them and later by others that the D-wave component of the deuteron is very important in the interference region, turning what would be a definite dip in the cross section into a shoulder. More detailed calculations by Franco and Glauber (ref. 30) and by Alberi and Bertocchi (ref. 31) produce excellent agreement with the 1 BeV p-D data and the π-d data from the European Organization for Nuclear Research (CERN).

With such increased knowledge about Glauber-type calculations, it would be very interesting to see if the present set of data at 580 MeV could be correctly predicted by taking spin and isospin dependence into account and by using the correct wave functions for the deuteron, ^{3}He, and ^{4}He; so far, this calculation has not been made.

In figure 20, preliminary calculations are shown of the p-^{4}He cross section and polarization at our energy by Ford and Pentz (ref. 22). Watson's multiple-scattering expansion is used to second order with an approximation in the double-scattering term. The spin- and isospin-dependent nucleon-nucleon scattering amplitudes are expressed as Gaussian functions of momentum transfer. The Gaussian functions are chosen by means of a least-square fit to the p-p and n-p cross section and polarization as predicted by the most recent Livermore phase shift analysis (ref. 10). For the ^{4}He particle wave function, the form used was one of the forms suggested by Bassel and Wilkin (refs. 4 and 5) which would yield a good fit to the single-particle form factor recently measured in Stanford. Since high-order scatterings are omitted, and the nucleon-nucleon amplitudes are oversimplified, there is no good agreement with the data, but the qualitative features are reproduced.

In an unpublished report, E. A. Remler of William and Mary University calculated the differential cross section and the polarization in p-D scattering near 580 MeV. His calculation is a straightforward application of Watson's theory in the impulse approximation and takes single-scattering and "direct" double-scattering terms into account. The transition operators describing the free nucleon-nucleon scattering were obtained from the Livermore phase shifts (ref. 10). A further ingredient for the calculation is the deuteron wave function. Remler used a rough fit to the Hamada-Johnston S-state wave function (ref. 32) as a sum of three Gaussians. The quadrupole form factor was

taken from Glendenning and Kramer (ref. 33) with a D-state probability altered to about 7 percent. The results are presented in figure 21. The three heavy lines correspond to calculations using the Hamada-Johnson S-state wave function. The heavy dashed curve represents single scattering only. The heavy broken curve represents single and double scattering without the D-state component. The heavy solid curve is the result when the D-state is included. Although the shape of the cross section and polarization angular distribution is reproduced, the magnitude is not. An excellent fit to the data at larger angles was obtained with a wave function that is peaked at a smaller radius than the Hamada-Johnston wave function (fig. 22). This may indicate the need for more high-momentum particles in the deuteron wave function. Since Remler plans to improve upon his calculation, this is a tentative result only. Another interesting result of Remler's calculation is the large effect of the D-state component on the polarization.

Experiments at Brookhaven in the energy region 1 to 1.5 GeV (refs. 2 and 11) have shown a large peaking of the p-D elastic cross section at 180°. Until recently, there has been no quantitative explanation for this fact. In a recent paper to be published in Physical Review Letters, Kerman and Kisslinger propose a model for the backward elastic p-D scattering at high energies. They start with the assumption that the basic mechanism is not a scattering collision, but a fermion transfer (pickup) process. This can be understood from momentum transfer considerations. The high-momentum Fourier component which the deuteron wave function would have to provide for a scattering collision makes this process quite unlikely. When calculating the cross section for such a pickup process in Born approximation using an S-state Hulthen wave function, the predictions for the backscattering cross section are too small by an order of magnitude. Better conventional wave functions (including the D-state component) help to increase the cross section, but by an insufficient amount. Kerman and Kisslinger see this result as an indication that there might be more involved than a single nucleon exchange mechanism. Considering that the nucleon-nucleon potential at close distances can be several hundred MeV deep, there is a considerable probability for the neutron or proton to be in an excited state. From a Regge model and a static field theory model, Kerman and Kisslinger suggest that the N*(1688) resonance, which has the same quantum number as the nucleon except for spin, may play an important role in the high-energy baryon transfer mechanism. With a momentum transfer, a different part of the momentum space deuteron wave function would be sampled. In figure 23, Kisslinger's predictions are compared with our large-angle data as a function of the momentum transferred in the pickup process Δ. The lower curve is the prediction of the calculation without D* (D* being the component of the deuteron wave function that includes the N* resonance). The upper curve is calculated with $2\frac{1}{2}$ percent D*, which, according to Kisslinger, is probably more than can be justified by the perturbation calculation. These results for the larger-angle scattering are quite encouraging. They show the usefulness of the high-energy pickup mechanism as a tool in nuclear structure.

Quasi-Elastic Large-Angle p-D Scattering

Intimately related to the large-angle p-D scattering is the production of high-momentum deuterons when nuclei are bombarded with high-energy protons. Many years ago, the authors of reference 34 studied the high-momentum spectra of particles produced by 675-MeV protons; they observed a small peak on the high-energy side of the elastically scattered protons. They concluded that these particles were deuterons produced by the collision of the incident protons with quasi-free neutron-proton pairs in the nuclei. The authors of reference 35 used the high-resolution magnetic spectrometer and a time-of-flight system of the cosmotron to investigate the deuteron production from ^{4}He, ^{6}Li, ^{12}C, ^{16}O, and natural lead bombarded with 1-GeV protons.

Since only one production cross section exists for atomic numbers A greater than 16 in the Brookhaven experiment, we have investigated the A dependence to larger values of A. The cross section for quasi-free p-D scattering was measured for nine nuclei between atomic numbers 3 and 208 at a deuteron angle of 12^{o} in the laboratory. The deuteron momentum spectra has been measured for ^{9}Be, ^{12}C, and natural lead. The spectrum for ^{9}Be is shown in figure 24. Even with the low momentum resolution of this experiment, the shift of the high momentum peak (attributed to quasi-elastic knock-out) in respect to the location of the free p-D scattering peak can be observed. The shift roughly corresponds to the 16.7-MeV binding energy of the deuteron in beryllium-9. The broad peak at lower momenta is probably connected with processes that produce pions along with the observed deuterons.

For the measurement of the quasi-free p-D cross section as a function of atomic number, the momentum window of the spectrometer Δp has been widened to accept the entire quasi-elastic peak. Deuterons with momenta below the threshold for pion production have been rejected. Obviously, this measurement cannot tell what final state the nuclei were left in, but the authors of reference 35 concluded from the results of a coincidence experiment that the residual nucleus ^{10}B of the (p, pD) reaction) was left at or near the ground state in most events. The results of these measurements are shown in figure 25. The cross sections are in excellent agreement with an $A^{1/3}$ dependence.

Lewis Research Center,
National Aeronautics and Space Administration,
Cleveland, Ohio, May 27, 1970,
129-02.

APPENDIX - RANDOM COINCIDENCE SUBTRACTION

Under normal beam extraction conditions, the instantaneous rate in any element of a range telescope was very large compared to the observed (average) rate. Consequently, large random coincidence rates were observed between sets of elements at very low average beam levels ($\sim 2 \times 10^7$ protons on target per sec). It was found that the observed triple- and higher-order coincidence rates contained random rates which could not be removed by simple chance coincidence subtraction, at least within the framework of the available electronic logic.

In this appendix, a scheme for removing the random coincidence contribution to an observed coincidence rate will be developed based on a model commensurate with the prevailing beam and electronic logic condition.

The time structure of the beam available from the SREL syncrocyclotron under normal extraction conditions is shown schematically in figure 6. The extracted beam has a macrostructure, as well as a microstructure. The macrostructure consists of groups of protons spilled from the cyclotron at a frequency $F = 54$ hertz with a duration $T =$ 50 to 200 microseconds. The duration of T depends on various cyclotron operating parameters. Within the macroburst, microbursts of protons of duration $t \approx 6$ nanoseconds occur with a frequency $f \approx 17$ megahertz (the cutoff frequency of the cyclotron). The microburst intensity envelope has a roughly isosceles triangular modulation of base T. The average number of protons spilled per macroburst appears to be relatively constant based on oscilloscope inspection of individual scintillation counter outputs, and only very long term variations in the total extracted beam occurred.

The electronic logic employed in this experiment used logic pulse widths of 6 nanoseconds, and all logic units recovered within about 12 nanoseconds. Consequently, a detector could produce only one logic pulse per microburst and that logic unit had recovered before the appearance of the next microburst. Measurements also showed that the average number of events in a detector was less than one per microburst.

Let the probability of detecting an event in detector i during the j^{th} microburst of a macroburst be

$$\left.\begin{aligned} p_{ij} &= A_i j^n \qquad 0 < j < \frac{Tf}{2} \\ p_{ij} &= A_i (Tf - j)^n \qquad \frac{Tf}{2} \leq j \leq Tf \end{aligned}\right\} \tag{A1}$$

where Tf is the number of microbursts per macroburst, A_i is a normalization constant, $p_{ij} << 1$ for all j's, and $n \geq 0$ is a form factor which describes the shape of the macroburst (i.e., when $n = 1$, the macroburst envelope has an isoceles triangular

shape). Equation (A1) describes an idealized beam which closely resembles the true cyclotron beam.

When equation (A1) is used, the average rate observed in detector i is

$$R_i = F \int_0^{Tf} p_{ij}\, dj = \frac{2A_i F}{n+1} \left(\frac{Tf}{2}\right)^{n+1} \tag{A2}$$

from which the constant A_i can be evaluated as

$$A_i = \frac{n+1}{2F} \frac{R_i}{\left(\frac{Tf}{2}\right)^{n+1}} \tag{A3}$$

The average random coincidence rate in two detectors, i and k, is

$$R^*_{ik} = F \int_0^{Tf} p_{ij} p_{kj} d_j = \frac{R_i R_k}{TFf} \frac{(n+1)^2}{2n+1} \tag{A4}$$

And by a similar calculation the average random triple coincidence rate is

$$R^*_{ik\ell} = \frac{R_i R_k R_\ell}{(TFf)^2} \frac{(n+1)^3}{3n+1} \tag{A5}$$

From equation (A4), an effective resolving time can be defined:

$$R^*_{ik} = gR_iR_k \qquad g = \frac{1}{TFf} \frac{(n+1)^2}{2n+1} \tag{A6}$$

And by rearrangement of equation (A5)

$$R^*_{ik\ell} = g^2 R_i R_k R_\ell \frac{(2n+1)^2}{(n+1)(3n+1)} \approx g^2 R_i R_k R_\ell \tag{A7}$$

since

$$1 < \frac{(2n+1)^2}{(n+1)(3n+1)} < 1.19 \qquad \text{for} \quad n \leq 2 \tag{A7}$$

Figures 26(a) to (c) show the possible first-order coincidences which can occur in a three-element charged-particle telescope in which elements 1 and 2 are much smaller than element 3 and an absorber is placed between elements 2 and 3. Higher-order coincidences can be neglected because a detector can only produce one logic pulse per microburst. Figure 26(a) shows a true coincidence event, figure 26(b) coincidences composed of both random and true events, and figure 26(c) a completely random event.

Let the average rates in the three elements of this telescope be R_1, R_2, and R_3. The observed triple coincidence rate will then be

$$R_{123} = R_{123T} + g(R_{12T}R_3 + R_{13T}R_2 + R_{23T}R_1) + \frac{g^2R_1R_2R_3(2n + 1)^2}{(n + 1)(3n + 1)} \tag{A8}$$

where the subscript T denotes a true rate.

The observed coincidence rates 1·2, 1·3, 2·3 will be

$$\left.\begin{aligned} R_{12} &= R_{12T} + gR_1R_2 \\ R_{23} &= R_{23T} + gR_2R_3 \\ R_{13} &= R_{13T} + gR_1R_3 \end{aligned}\right\} \tag{A9}$$

Equation (A9) and the approximation of equation (A7) are used to rewrite equation (A8) as follows:

$$R_{123} \approx R_{123T} + g(R_{12}R_3 + R_{13}R_2 + R_{23}R_1) - 2g^2R_1R_2R_3 \tag{A10}$$

If a portion of the electronic logic is arranged so that the information from detector 3, for instance, arrives at a triple coincidence circuit delayed one microburst from the information from detectors 1 and 2, the random coincidence rate $R^*_{12(3)}$ that exists between events in detector 3 and observed coincidences in 1·2 will be measured

$$R^*_{12(3)} = gR_{12}R_3$$

and knowing R_{12} and R_3, g is determined

$$g = \frac{R^*_{12(3)}}{R_{12}R_3} \tag{A11}$$

Substituting this value of g in equation (A10) results in

$$R_{123} = R_{123T} + R^*_{12(3)}\left[(1 + C_1 + C_2) - 2C_3\right] \tag{A12}$$

where

$$C_1 = \frac{R_{13}R_2}{R_{12}R_3}$$

$$C_2 = \frac{R_{23}R_1}{R_{12}R_3}$$

$$C_3 = \frac{R^*_{12(3)}R_1R_2}{(R_{12})^2R_3}$$

Equation (A12) then allows R_{123T} to be calculated from R_{123} observed, if $R^*_{12(3)}$ and the rates necessary to compute C_1, C_2, and C_3 are known.

The telescope used in this experiment consisted of seven elements. The last five elements were equal in size, closely spaced, and much larger than elements 1 and 2. Because of the large size and close spacing of elements 3 to 7, a particle which passed through element 3 very likely passed through elements 4 to 7 if it did not stop somewhere before element 7.

The electronic logic employed throughout these experiments is shown in figure 5. A coincidence 123 . . . n is formed by a coincidence between 123 . . . n - 1 and events in n. If the particle which produces an event in n participated in a chance coincidence event in 123 . . . n - 1, it will produce a chance coincidence event in 123 . . . n. Consequently, random subtraction for coincidences of the sort 1·2·3 . . . n could not be analyzed on a simple chance basis. It is evident that random events shown in figures 26(b-1) and (c) are carried into coincidence 123 . . . n, as random events, in a proportion $R_{3\ldots n}/R_3$, and that the random events shown in figures 26(b-2) and (b-3) are carried into coincidence 1·2·3 . . . n, as random events, in a proportion $R_{123\ldots nT}/R_{123T}$. In addition, those coincident events observed in coincidence circuit 123 . . . n - 1 can be in chance coincidence with events in detector n.

The observed coincidence rate R_{1234} will equal the true rate R_{1234T} plus the chance rate due to events of the sort shown in figures 26(b-1) and (c),

$$\left(gR_{12T}R_3 + g^2R_1R_2R_3\right)\frac{R_{34}}{R_3} = R^*_{12(3)}\,\frac{R_{34}}{R_3} \tag{A13}$$

plus the chance rate due to events of the sort shown in figures 26(b-2) and (b-3),

$$(gR_{23T}R_1 + gR_{13T}R_2)\frac{R_{1234T}}{R_{123T}} = R^*_{12(3)}(C_1 + C_2 - 2C_3)\frac{R_{1234T}}{R_{123T}} \tag{A14}$$

plus the chance rate between events 1·2·3 and events in detector 4,

$$R_{123}gR_4 = R^*_{12(3)}\frac{R_{123}R_4}{R_{12}R_3} \tag{A15}$$

Therefore,

$$R_{1234} = R_{1234T} + R^*_{12(3)}\left[\frac{R_{34}}{R_3} + (C_1 + C_2 - 2C_3)\frac{R_{1234T}}{R_{123T}} + \frac{R_{123}}{R_{12}}\frac{R_4}{R_3}\right] \tag{A16}$$

Experimentally,

$$\frac{R_{123}R_4}{R_{12}R_3} << \frac{R_{34}}{R_3} \approx (C_1 + C_2 - 2C_3)\frac{R_{1234T}}{R_{123T}} \tag{A17}$$

The true rate at which particles penetrate elements 1 to 4 can therefore be evaluated:

$$R_{1234T} = \frac{R_{1234} - R^*_{12(3)}\dfrac{R_{34}}{R_3}}{1 + (C_1 + C_2 - 2C_3)\dfrac{R^*_{12(3)}}{R_{123T}}} \tag{A18}$$

and, in general, it can then be shown that

$$R_{123\ldots nT} = \frac{R_{123\ldots n} - R^*_{12(3)}\dfrac{R_{3\ldots n}}{R_3}}{1 + \dfrac{R^*_{12(3)}}{R_{123T}}(C_1 + C_2 - 2C_3)} \tag{A19}$$

It is obvious from the block diagram of the electronics (fig. 5) that not all the information necessary to calculate the true rate at which particles penetrate the elements of the telescope from equations (A12) and (A19) was recorded. However, throughout the

experiment, auxiliary measurements were made by changing the logic requirements such that C_1, C_2, C_3, $R_{3...n}$, and R_3 were known.

To test this method of calculating random coincidences, a series of measurements were performed at various beam levels for a number of counter geometries. An extrapolation to zero beam level gave the true coincidence rates for each configuration. At the highest beam level and with the worst experimental configuration, random coincidences accounted for one-half of the observed events. When the method outlined on the preceding pages was used, the calculated random coincidence rates for all configurations and beam levels was between 80 and 100 percent of the expected random rates.

REFERENCES

1. Palevsky, H.; Friedes, J. L.; Sutter, R. J.; Bennett, G. W.; Igo, G. J.; Simpson, W. D.; Phillips, G. C.; Corley, D. M.; Wall, N. S.; Stearns, R. L.; and Gottschalk, B.: Helium, Carbon, and Oxygen Nuclei. Phys. Rev. Letters, vol. 18, no. 26, June 26, 1967, pp. 1200-1204.

2. Bennett, G. W.; Friedes, J. L.; Palevsky, H.; Sutter, R. J.; Igo, G. J.; Simpson, W. D.; Phillips, G. C.; Stearns, R. L.; and Corley, D. M.: Proton-Deuteron Scattering at 1 BeV. Phys. Rev. Letters, vol. 19, no. 7, Aug. 14, 1967, pp. 387-390.

3. Czyz, W.; and Leśniak, L.: Elastic Scattering of Very High Energy Particles from Nuclei. Phys. Letters, vol. 24B, no. 5, Mar. 6, 1967, pp. 227-229.

4. Bassel, R. H.; and Wilkin, C.: Structure of the α Particle from Elastic Proton Scattering. Phys. Rev. Letters, vol. 18, no. 20, May 15, 1967, pp. 871-873.

5. Bassel, Robert H.; and Wilkin, Colin: High-Energy Proton Scattering and the Structure of Light Nuclei. Phys. Rev., vol. 174, no. 4, Oct. 20, 1968, pp. 1179-1199.

6. Glauber, R. J.: High-Energy Collision Theory. Lectures in Theoretical Physics. Vol. 1. W. E. Brittin and L. G. Dunham, eds., Interscience Publishers, 1959, pp. 315-414.

7. Cheng, David: Nucleon-Nucleon Polarization at 700, 600, 500, and 400 MeV. Rep. UCRL-11926, California Univ. Lawrence Radiation Lab., July 1, 1965.

8. Azhgireĭ, L. S.; et al.: Measurement of Polarization in 667-MeV p-p Scattering. Soviet J. Nucl. Phys., vol. 2, no. 5, May 1966, pp. 636-638.

9. Cumming, J. B.; Hudis, J.; Poskanzer, A. M.; and Kaufman, S.: $Al^{27}(p,3pn)Na^{24}/C^{12}(p,pn)C^{11}$ Cross-Section Ratio in the GeV Region. Phys. Rev., vol. 128, no. 5, Dec. 1, 1962, pp. 2392-2397.

10. MacGregor, Malcom H.; Arndt, Richard A.; and Wright, Robert M.: Determination of the Nucleon-Nucleon Scattering Matrix. VIII. (p,p) Analysis from 350 to 750 MeV. Phys. Rev., vol. 169, no. 5, May 25, 1968, pp. 1149-1166.

11. Coleman, E.; Heinz, R. M.; Overseth, O. E.; and Pellett, D. E.: Proton-Deuteron Elastic Scattering at High Momentum Transfers. Phys. Rev. Letters, vol. 16, no. 17, Apr. 25, 1966, pp. 761-763.

12. Formánek, J.; and Trefil, J. S.: On the Possibility of Obtaining Particle Scattering Amplitudes from Nuclear Scattering Processes. Nucl. Phys., vol. B3, 1967, pp. 155-172.

13. Formánek, J.; and Trefil, J. S.: Determination of Particle Scattering Amplitudes from Nuclear Photoproduction. Nucl. Phys., vol. B4, 1967, pp. 165-179.

14. Durand, Loyal, III; and Lipes, Richard: Diffraction Model for High-Energy pp Scattering. Phys. Rev. Letters, vol. 20, no. 12, Mar. 18, 1968, pp. 637-640.

15. Chou, T. T.; and Yang, C. N.: Model of Elastic High-Energy Scattering. Phys. Rev., vol. 170, no. 5, June 25, 1968, pp. 1591-1596.

16. Chou, T. T.; and Yang, C. N.: Model of High-Energy Elastic Scattering and Diffractive Excitation Processes in Hadron-Hadron Collisions. Phys. Rev., vol. 175, no. 5, Nov. 25, 1968, pp. 1832-1834.

17. Schiff, L. I.: High-Energy Scattering at Moderately Large Angles. Phys. Rev., vol. 176, no. 4, Dec. 20, 1968, pp. 1390-1394.

18. Ross, D. K.: High-Energy Multiple Scattering for Large Angles. Phys. Rev., vol. 173, no. 5, Sept. 25, 1968, pp. 1695-1699.

19. Goldberger, Marvin L.; and Watson, Kenneth M.: Collision Theory. John Wiley & Sons, Inc., 1964, Ch. 11.

20. Pumplin, Jon: Elastic Scattering from Deuteron. Phys. Rev., vol. 173, no. 5, Sept. 25, 1968, pp. 1651-1659.

21. Remler, Edward A.: High-Energy Scattering by Nuclei. Phys. Rev., vol. 176, no. 5, Dec. 25, 1968, pp. 2108-2112.

22. Ford, William F.; and Pentz, Norman E.: A Large-Angle Approximation for High-Energy Scattering. Presented at the American Physical Society Meeting, Washington, D.C., Apr. 28-May 1, 1969.

23. Frosch, R. F.; McCarthy, J. S.; Rand, R. E.; and Yearian, M. R.: Structure of the He^4 Nucleus from Elastic Electron Scattering. Phys. Rev., vol. 160, no. 4, Aug. 20, 1967, pp. 874-879.

24. Glauber, R. J.: Theoretical Aspects of Experiments Using High-Energy Protons. Proceedings of the Symposium on the Use of NIMROD for Nuclear Structure Physics. C. J. Batty, ed. Rep. RHEL/R-166, Rutherford High Energy Lab., England (AEC Rep. CONF-680314), June 1968, pp. 41-65.

25. Czyz, W.; and Lesniak, L.: Elastic Electron Scattering from Nuclei and Nucleon-Nucleon Correlations. Rep. INR-540/PL, Institute for Nuclear Research, Poland, Apr. 1967.

26. Franco, Victor: Scattering of Protons by Deuterium and Helium. Phys. Rev. Letters, vol. 21, no. 18, Oct. 28, 1968, pp. 1360-1364.

27. Kujawski, E.; Sachs, David; and Trefil, J. S.: Spin Effects in the Scattering of Protons from Light Nuclei and a Possible Test for the Existence of Regge Cuts. Phys. Rev. Letters, vol. 21, no. 8, Aug. 19, 1968, pp. 583-585.

28. Harrington, David R.: D-Wave Effects in High-Energy Proton-Deuteron Scattering. Phys. Rev. Letters, vol. 21, no. 21, Nov. 18, 1968, pp. 1496-1498.

29. Coleman, E.; and Rhoades, T. G.: Effect of D-State in Deuterium Scattering. Minnesota Univ. (AEC Rep. COO-1764-19), Oct. 29, 1968.

30. Franco, Victor and Glauber, Roy J.: Effect of Quadrupole Deformation on High-Energy Scattering of Deuterons. Phys. Rev. Letters, vol. 22, no. 8, Feb. 24, 1969, pp. 370-374.

31. Alberi, G.; and Bertocchi, L.: Glauber Shadow and Inelastic Contributions to πd Scattering. Nuovo Cimento, vol. 61A, no. 2, May 21, 1969, pp. 203-214.

32. Hamada, T.; and Johnston, I. D.: A Potential Model Representation of Two-Nucleon Data below 315 MeV. Nucl. Phys., vol. 34, 1962, pp. 382-403.

33. Glendenning, Norman K.; and Kramer, Gustav: Nucleon-Nucleon Triplet-Even Potentials. Phys. Rev., vol. 126, no. 6, June 15, pp. 2159-2168.

34. Azhgireĭ, L. S.; Vzorov, I. K.; Zrelov, V. P.; Mescheriakov, M. G.; Neganov, B. S.; and Shabudin, A. F.: Knockout of Deuterons from Li, Be, C, and O Nuclei by Protons of Energy 675 MeV. Soviet Phys.-JETP, vol. 6, no. 5, May 1958, pp. 911-919.

35. Sutter, R. J.; Friedes, J. L.; Palevsky, H.; Bennett, G. W.; Igo, G. J.; Simpson, W. D.; Phillips, G. C.; Corley, D. M.; Wall, N. S.; and Stearns, R. L.: Production of High-Momentum Deuterons from Nuclei Bombarded by 1-BeV Protons. Phys. Rev. Letters, vol. 19, no. 20, Nov. 13, 1967, pp. 1189-1191.

TABLE I. - p-p DIFFERENTIAL CROSS SECTION

AT 582 MeV

Proton center-of-mass scattering angle, $\theta_{p,cm}$, deg	Center-of-mass differential cross section and error, $\left(\frac{d\sigma}{d\Omega}\right)_{cm} \pm \Delta\left(\frac{d\sigma}{d\Omega}\right)_{cm}$, mb/sr
15	5.98±0.25
20	5.91±0.18
27.4	5.45±0.16
[a]27.4	5.78±0.21
30	5.13±0.10
30	5.40±0.09
40	4.55±0.08
50	3.95±0.09
60	3.47±0.06
70	2.72±0.05
80	2.80±0.06
90	2.58±0.05
[b]90	2.53±0.07

[a]Measured with time-of-flight system.

[b]Measured with a gas target.

TABLE II. - p-D DIFFERENTIAL CROSS SECTION AT 582 MeV

Proton laboratory scattering angle, $\theta_{p, lab}$, deg	Momentum transfer squared, -t, $(GeV/c)^2$	Laboratory differential cross section and error, $\left(\frac{d\sigma}{d\Omega}\right)_{lab} \pm \Delta\left(\frac{d\sigma}{d\Omega}\right)_{lab}$, mb/sr	Proton center-of-mass scattering angle, $\theta_{p, cm}$, deg	Center-of-mass differential cross section and error, $\left(\frac{d\sigma}{d\Omega}\right)_{cm} \pm \Delta\left(\frac{d\sigma}{d\Omega}\right)_{cm}$, mb/sr
10	0.044	33.5±5.4	16.9	11.9±1.9
12	.062	21.5±1.7	20.3	7.7±0.6
[a]12	.062	19.2±1.7	20.3	6.9±0.6
15	.092	10.0±1.6	25.3	3.7±0.6
17	.123	8.4±1.4	28.6	3.1±0.5
20	.167	3.25±0.3	33.6	1.24±0.10
22	.195	2.1±0.2	36.8	.82±0.07
25	.250	.95±0.05	41.7	.38±0.02
27	.285	.64±0.05	44.9	.27±0.02
30	.347	.37±0.02	49.6	.15±0.01
32	.395	.26±0.03	52.8	.11±0.01
35	.465	.20±0.01	57.4	.091±0.005
37	.520	.18±0.01	60.5	.081±0.005
40	.575	.19±0.01	65.0	.091±0.005
45	.690	.16±0.01	72.7	.083±0.005
50	.81	.125±0.005	79.5	.071±0.003
55	.94	.089±0.010	86.2	.055±0.003
60	1.07	.066±0.003	92.7	.045±0.002
65	1.17	.051±0.007	99.0	.039±0.005
70	1.27	.033±0.002	104.9	.028±0.002
75	1.36	.024±0.003	110.6	.023±0.002
80	1.45	.021±0.002	116.0	.022±0.002
90	1.61	.018±0.002	126.0	.024±0.003
100	1.72	.023±0.002	134.8	.037±0.003
110	1.80	.034±0.003	142.5	.071±0.007
120	1.87	.045±0.003	149.5	.117±0.018
[a]127	1.91	.040±0.003	154.0	.121±0.009
130	1.93	.053±0.003	155.6	.172±0.008
140	1.97	.045±0.002	161.2	.168±0.007
150	2.01	.040±0.006	166.2	.172±0.026

[a]Measured with time-of-flight system.

TABLE III. - p-D POLARIZATION AT 544 MeV

Proton laboratory scattering angle, $\theta_{p, lab}$, deg	Momentum transfer squared, -t, $(GeV/c)^2$	Polarization and error, P ± ΔP	Center-of-mass scattering angle, θ_{cm}, deg
10	0.038	0.484±0.091	16.8
15	.089	.535±0.028	25.1
20	.153	.482±0.035	33.3
25	.238	.267±0.102	41.3
30	.324	-.051±0.068	49.2
35	.419	-.304±0.056	56.9
40	.523	-.149±0.075	64.5
45	.643	-.135±0.105	71.8
49	.728	.025±0.070	77.5
60	.952	-.058±0.077	92.2
70	1.156	-.061±0.084	104.4
80	1.321	.010±0.140	116.0
90	1.457	-.074±0.115	125.5

TABLE IV. - p-^{3}He DIFFERENTIAL CROSS SECTION AT 582 MeV

Proton laboratory scattering angle, $\theta_{p, lab}$, deg	Momentum transfer squared, -t, $(GeV/c)^2$	Laboratory differential cross section and error, $\left(\frac{d\sigma}{d\Omega}\right)_{lab} \pm \Delta\left(\frac{d\sigma}{d\Omega}\right)_{lab}$, mb/sr	Proton center-of-mass scattering, angle, $\theta_{p, cm}$, deg	Center-of-mass differential cross section and error, $\left(\frac{d\sigma}{d\Omega}\right)_{cm} \pm \Delta\left(\frac{d\sigma}{d\Omega}\right)_{cm}$, mb/sr
17	0.122	7.15±0.64	24.7	3.40±0.30
19	.152	3.15±0.38	27.6	1.52±0.18
20	.168	1.34±0.26	29.0	.65±0.13
21	.185	1.52±0.11	32.5	.74±0.05
23	.219	.43±0.043	33.4	.211±0.021
24	.237	.32±0.10	34.7	.159±0.050
25	.256	.121±0.010	36.1	.061±0.005
26.5	.286	.078±0.009	38.2	.039±0.005
28	.317	.075±0.008	40.3	.038±0.004
30	.360	.074±0.008	43.1	.038±0.004
33	.427	.080±0.006	47.2	.043±0.003
35	.476	.082±0.005	49.9	.044±0.003
37	.522	.065±0.0065	52.6	.036±0.004
40	.600	.046±0.005	56.6	.026±0.003
42	.652	.040±0.005	59.3	.023±0.003
45	.732	.045±0.023	63.2	.027±0.014

TABLE V. - p-^{4}He ELASTIC CROSS SECTIONS AT 587 MeV

Proton laboratory scattering angle, $\theta_{p, lab}$, deg	Momentum transfer squared, -t, $(GeV/c)^2$	Laboratory differential cross section and error, $\left(\frac{d\sigma}{d\Omega}\right)_{lab} \pm \Delta\left(\frac{d\sigma}{d\Omega}\right)_{lab}$, mb/sr	Proton center-of-mass scattering angle, $\theta_{p, cm}$, deg	Center-of-mass differential cross section and error, $\left(\frac{d\sigma}{d\Omega}\right)_{cm} \pm \Delta\left(\frac{d\sigma}{d\Omega}\right)_{cm}$, mb/sr
4	0.007	409±45	5.4	210±23
5	.011	345±37	6.85	180±19
6	.016	276±30	8.0	145±16
7	.022	232±25	9.5	124±13
8	.028	201±24	11.0	106±13
9	.035	177±19	12.3	94±0.10
10	.043	133±15	13.7	71±0.8
11	.052	111±12	14.9	59±6.5
12	.062	87±9.5	16.25	47.5±5.2
13	.073	70±7.5	17.7	38±4.1
14	.085	48.5±4.9	19.2	26.4±2.7
15	.097	33.0±3.5	20.65	18.0±1.9
17	.124	17.7±2.0	23.2	9.8±1.1
19	.157	6.7±0.8	25.65	3.8±0.5
20	.170	4.0±0.4	26.9	2.28±0.23
21	.190	2.5±0.26	28.25	1.43±0.15
23	.225	1.03±0.13	31.0	.68±0.08
24	.245	.60±0.07	32.5	.35±0.04
25	.265	.43±0.06	33.85	.25±0.04
26	.28	.31±0.10	35.2	.19±0.06
27	.30	.28±0.05	36.4	.17±0.03
28	.325	.41±0.04	37.7	.25±0.025
29	.35	.40±0.04	39.1	.25±0.025
30	.37	.57±0.05	40.4	.35±0.030
31	.39	.46±0.04	41.9	.28±0.03
32	.41	.45±0.05	43.0	.28±0.03
34	.47	.36±0.06	45.6	.23±0.04
36	.52	.29±0.03	48.2	.19±0.02
38	.57	.23±0.03	50.8	.15±0.02
39	.60	.18±0.018	52.1	.12±0.012
40	.63	.13±0.01	53.3	.086±0.006
42	.67	.095±0.005	55.8	.064±0.004
44	.74	.081±0.009	58.2	.056±0.006
46	.80	.050±0.01	60.8	.035±0.007
48	.86	.031±0.007	63.25	.022±0.005
50	.92	.019±0.005	65.7	.014±0.004
55	1.07	.012±0.004	71.8	.009±0.003
60	1.23	.012±0.006	77.9	.0095±0.005

TABLE VI. - p-^{4}He POLARIZATION AT 540 MeV

Proton laboratory scattering angle, $\theta_{p, lab}$, deg	Proton center-of-mass scattering angle, $\theta_{p, cm}$, deg	Momentum transfer squared, -t, $(GeV/c)^2$	Polarization and error, $P \pm \Delta P$
4	5.4	0.006	0.286±0.108
6	8.2	.014	.385±0.028
8	10.9	.025	.485±0.031
10	13.6	.039	.536±0.015
12	16.4	.057	.475±0.032
15	20.4	.088	.451±0.029
17	23.1	.112	.365±0.015
20	27.1	.153	.154±0.040
22	29.8	.186	.049±0.056
23	31.1	.202	.044±0.066
25	33.7	.236	-.160±0.056
27	36.3	.272	.145±0.065
30	40.3	.332	.305±0.078
34	45.5	.420	.483±0.103
38	50.6	.512	.476±0.073
42	55.6	.610	.453±0.117

TABLE VII. - RANGE OF RELATIVE AND ABSOLUTE ERRORS

Reaction	Relative error, percent					Absolute error, percent	Accumulated absolute error, percent
	Scatter rate, N	Efficiency, ϵ	Nuclear density, ρ	Geometry factor, $G(\theta)$		Flux calibration, φ	
				Target orientation	Solid angle		
p-p	1 to 3.5	1	<1	0 to 1.7	2	5.9	6.2
p-D	4 to 16	1 to 10	<1	0 to 1.7	2	6.5	6.8
p-^{3}He	4 to 20	4 to 9	4	-------	4	6.6	7.7
p-^{4}He	4 to 20	4 to 10	<1	-------	4	6.4	7.5
p-p[a]	2.5	1	<1	0.4	1	5.9	6.2
p-D[a]	6 to 10	1	<1	.4	1	5.9	6.2

[a]Time-of-flight measurement.

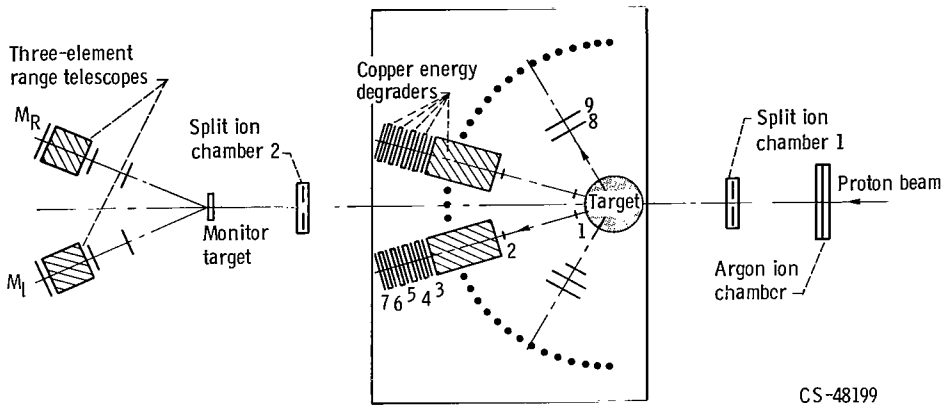

Figure 1. - Arrangement of experiment in proton target area (PTA).

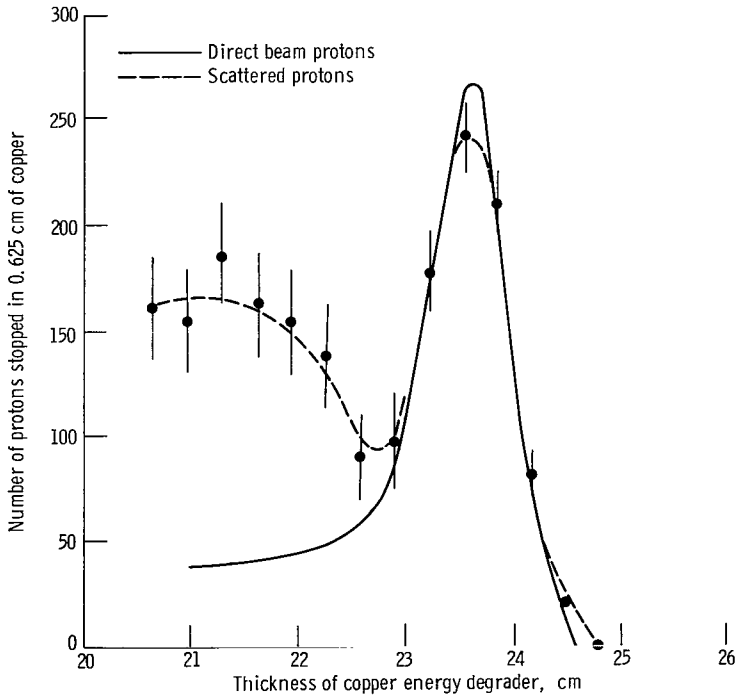

Figure 2. - Differential range curve of direct and scattered 574-MeV protons.

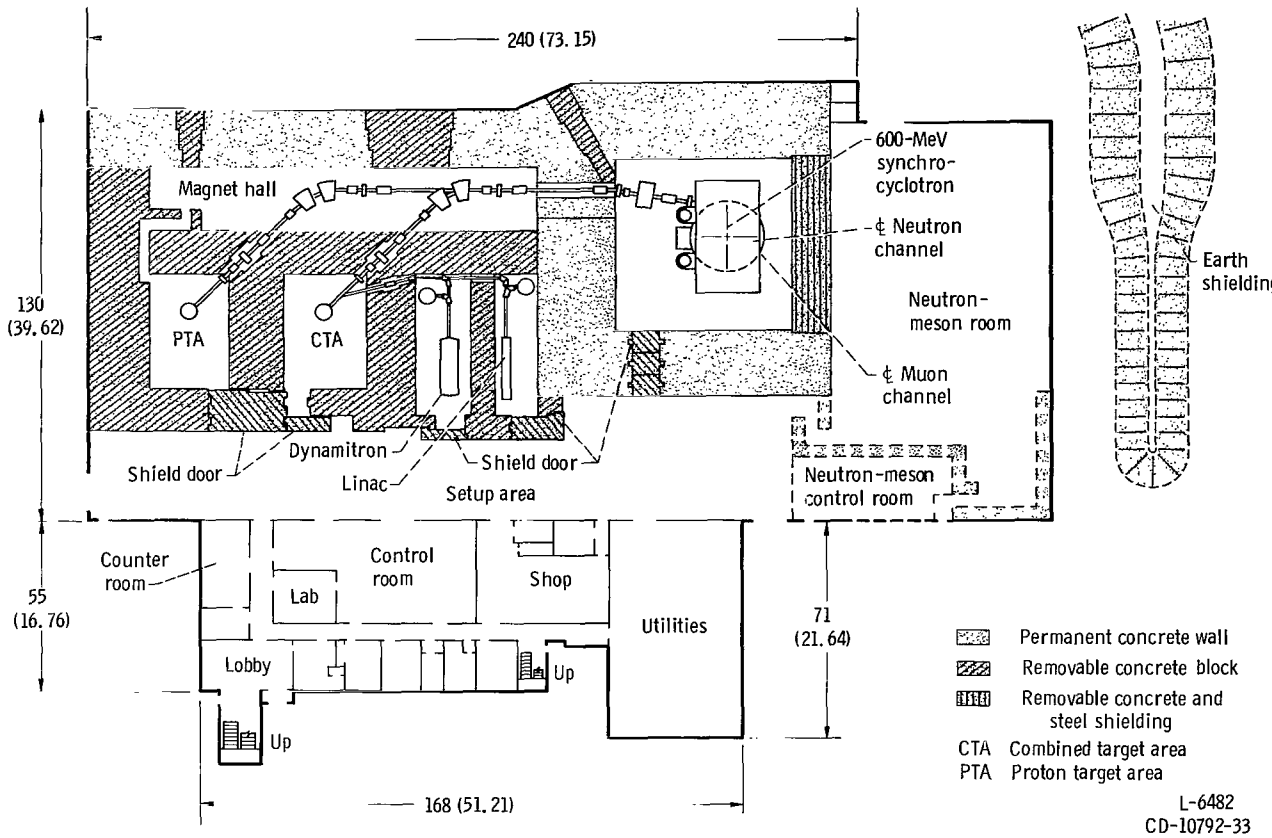

Figure 3. - Plan view of NASA Space Radiation Effects Laboratory (SREL). (All dimensions are in feet (m)).

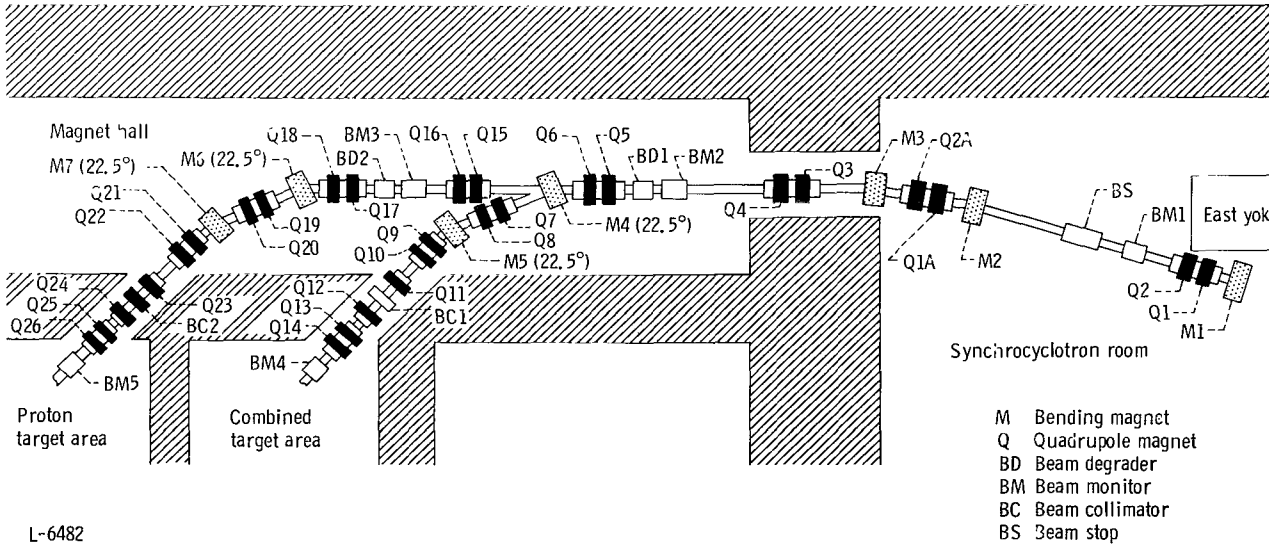

Figure 4. - Schematic diagram of proton beam transport system of SREL.

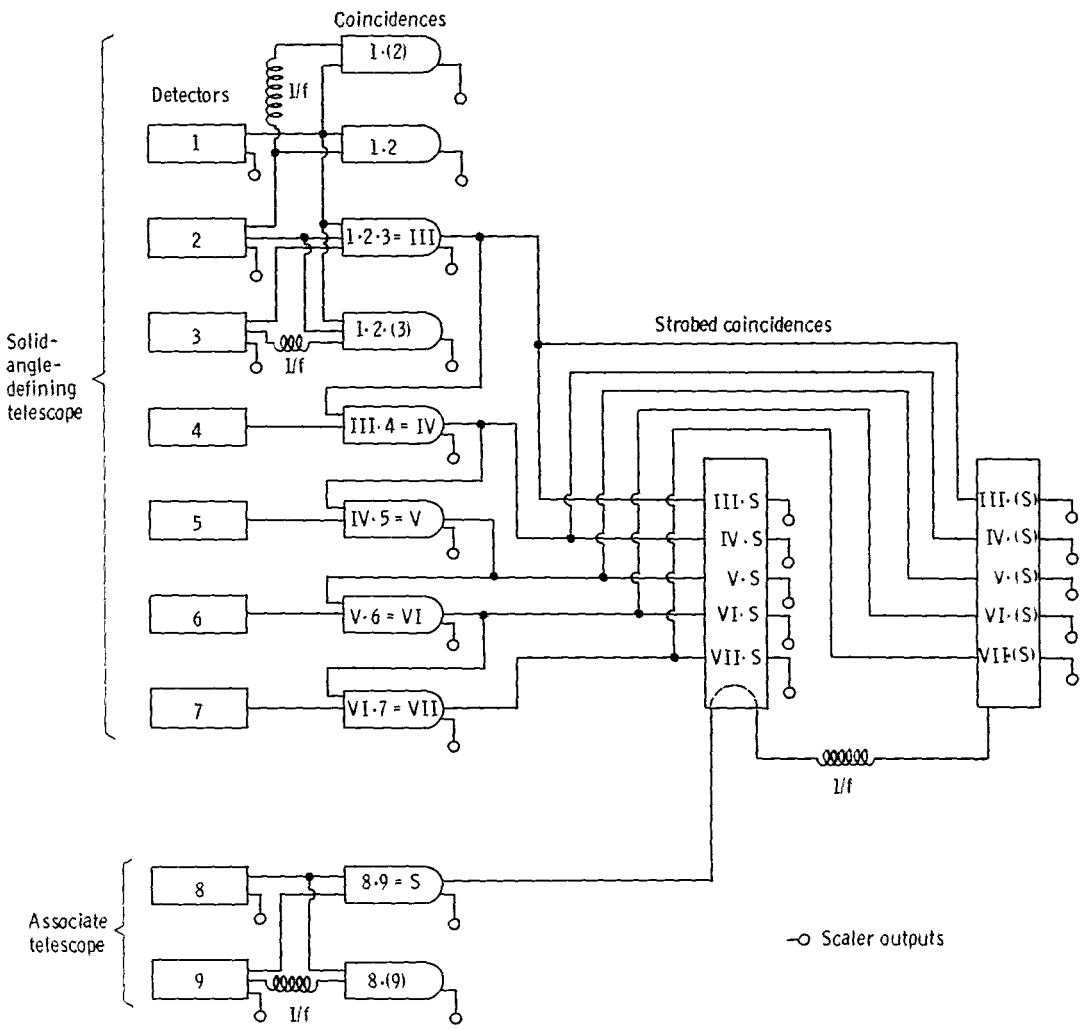

Figure 5. - Block diagram of differential cross section and polarization electronics.

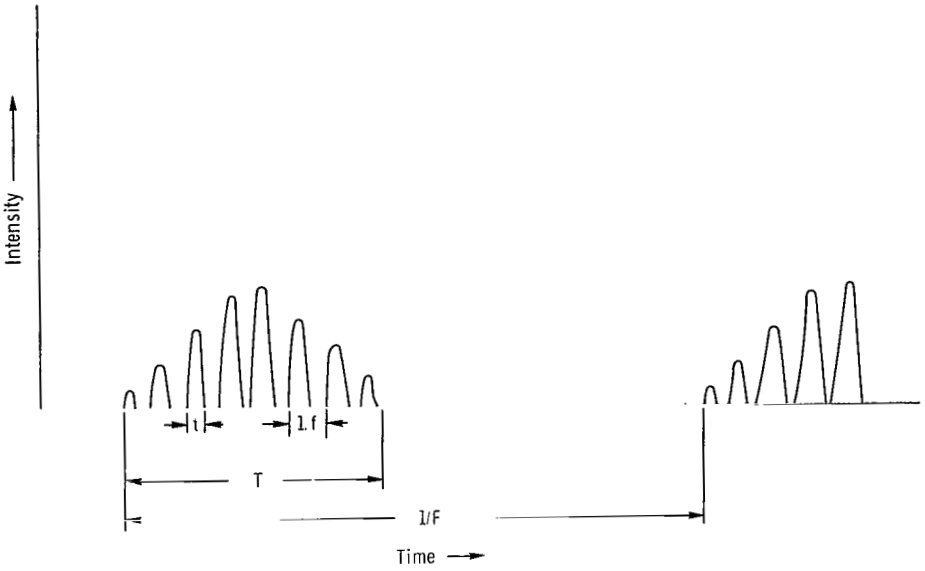

Figure 6. - Schematic time structure of normally extracted proton beam.

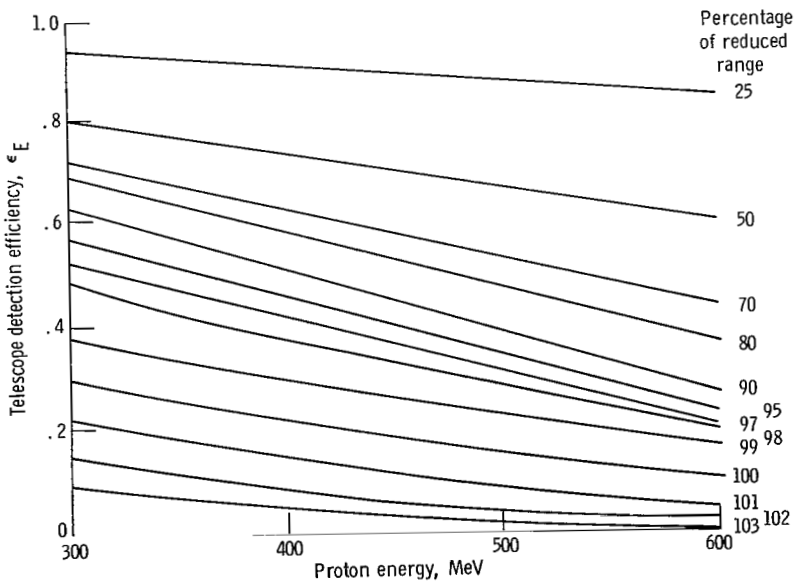

Figure 7. - Proton telescope detection efficiency as function of energy and reduced range.

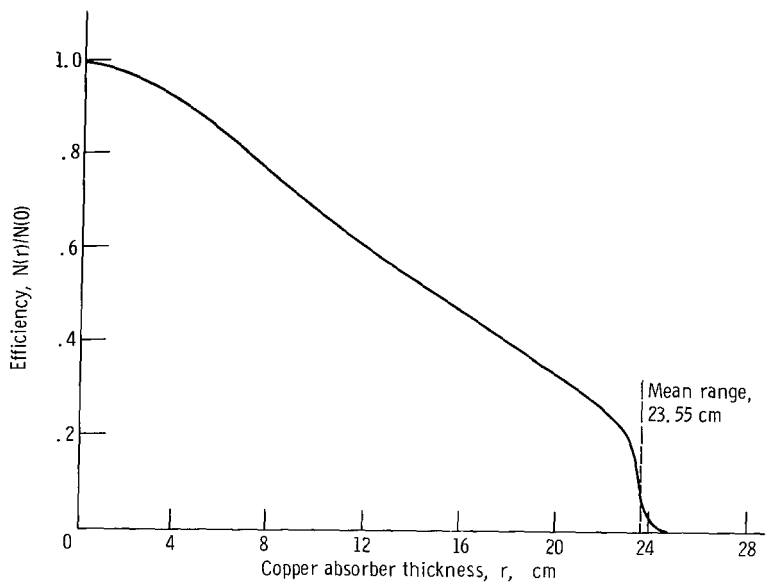

Figure 8. - Integral range curve of 574-MeV protons in copper.

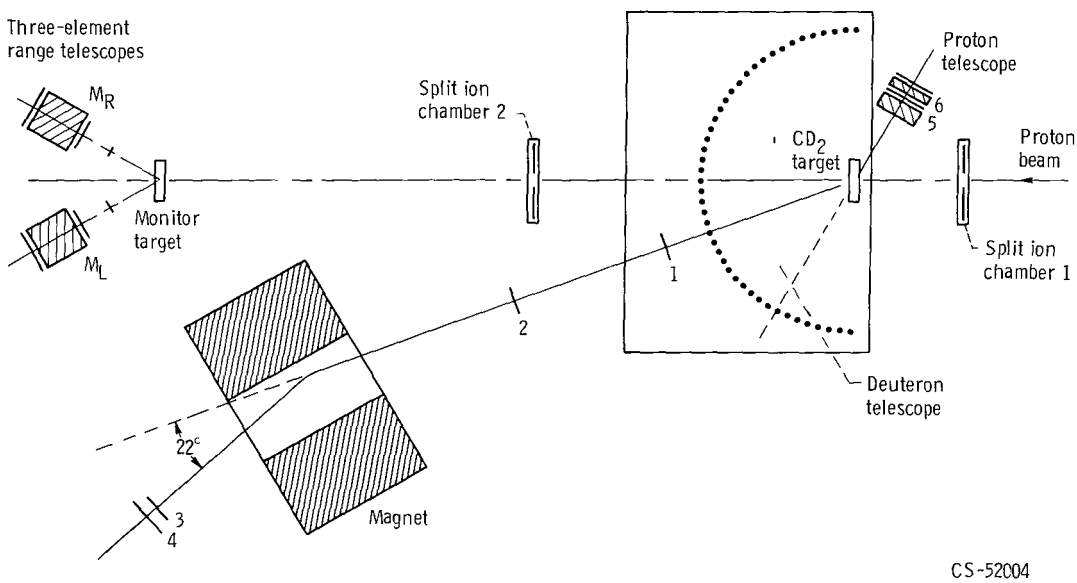

Figure 9. - Experimental arrangement of time-of-flight system.

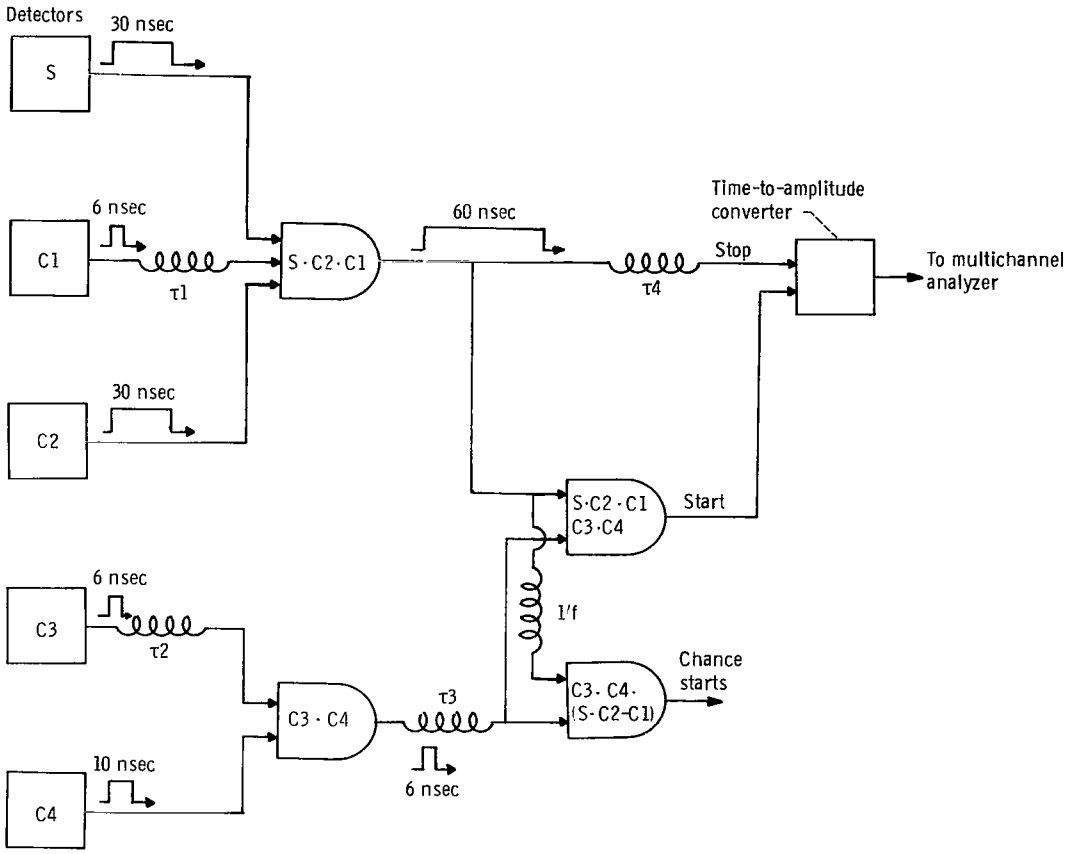

Figure 10. - Block diagram of time-of-flight electronics.

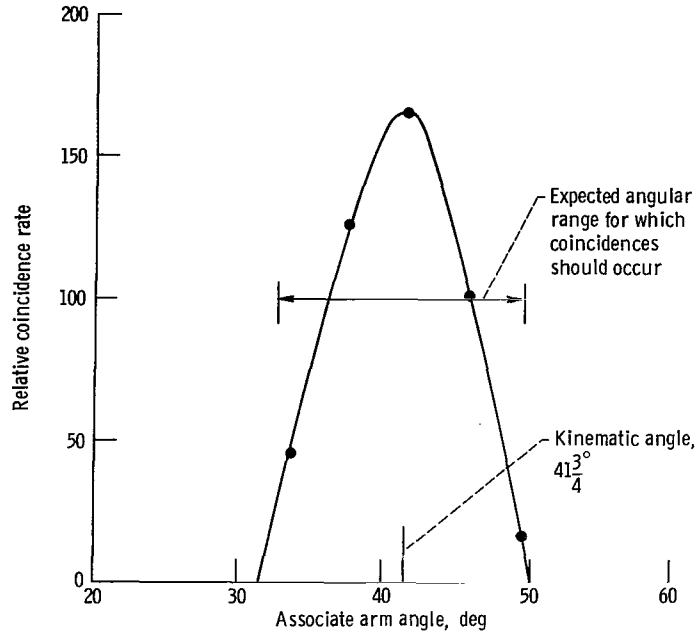

Figure 11. - Associate telescope coincidence rate as function of deuteron telescope angle for fixed proton telescope angle of 60° laboratory angle.

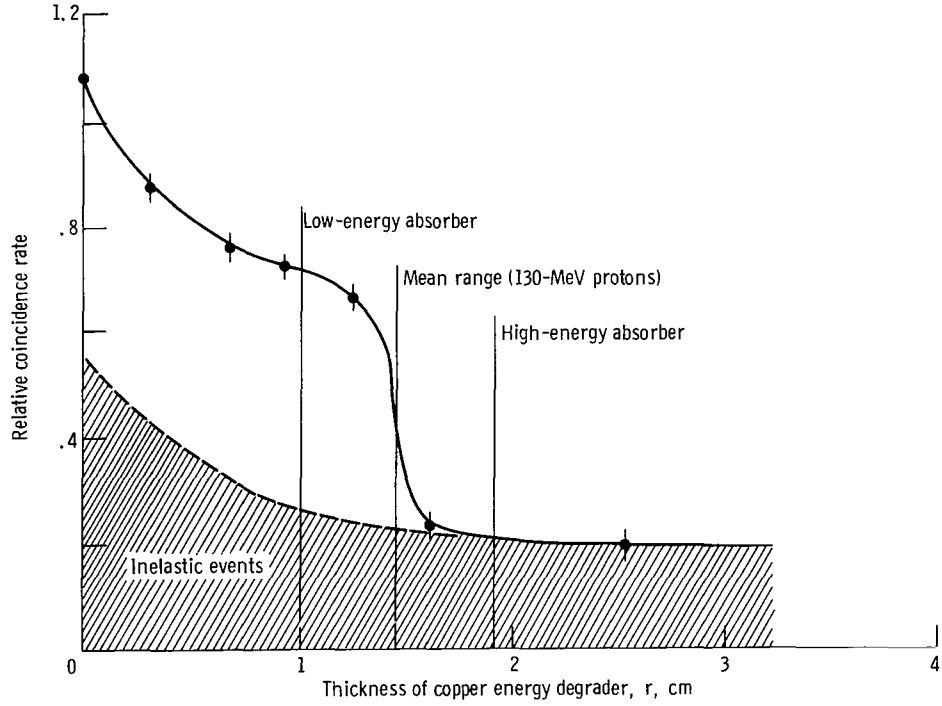

Figure 12. - Proton range curve for protons scattered through 100° laboratory angle.

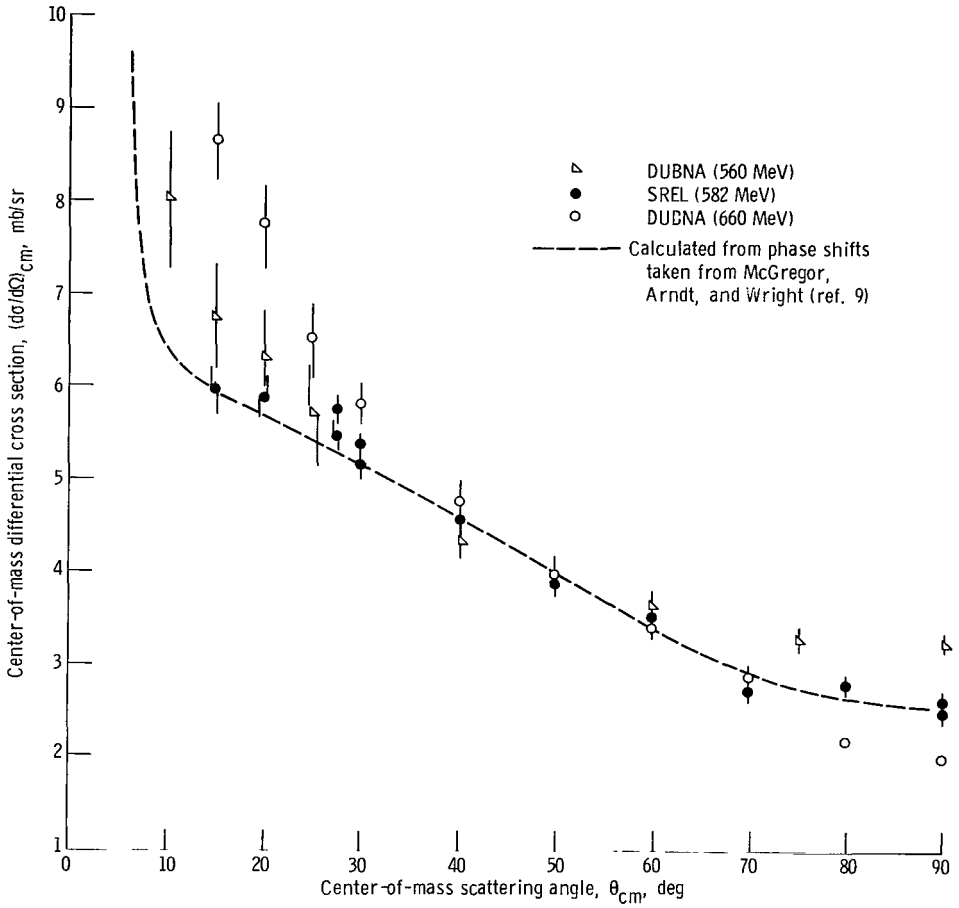

Figure 13. - p-p differential cross section as function of center-of-mass scattering angle.

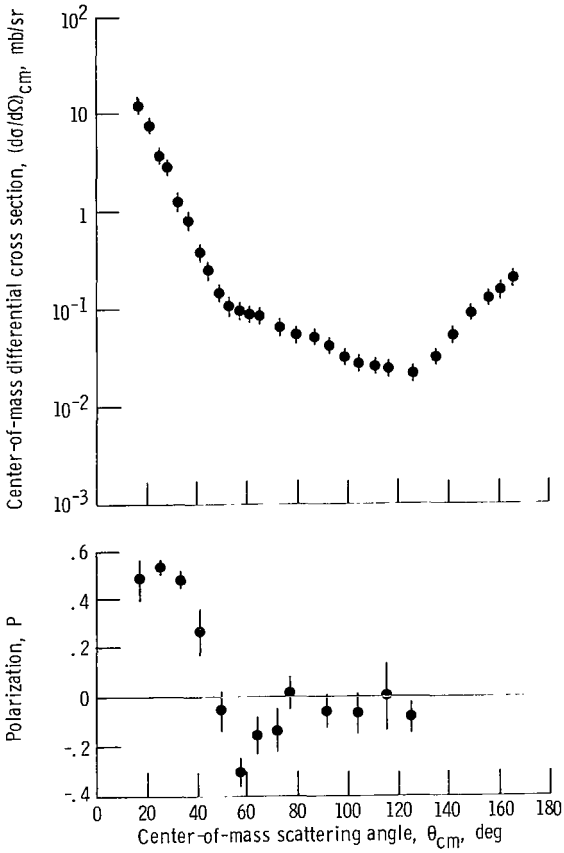

Figure 14. - p-D differential cross section and polarization as function of center-of-mass scattering angle, at 582 MeV.

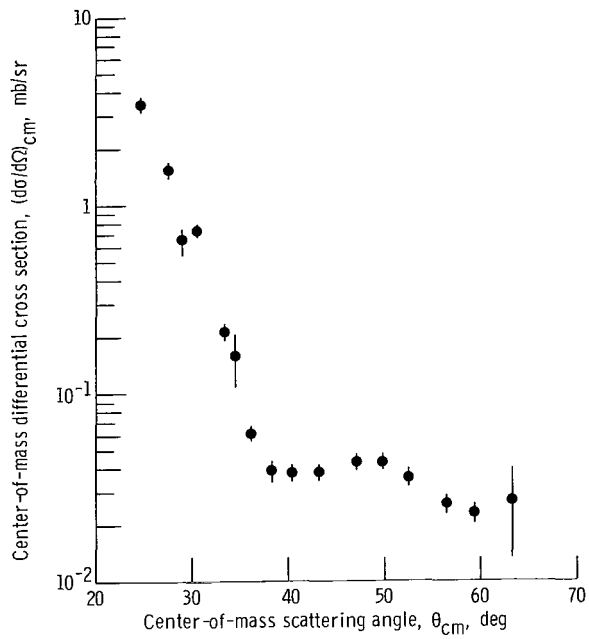

Figure 15. - p-^{3}He differential cross section as function of center-of-mass scattering angle, at 587 MeV.

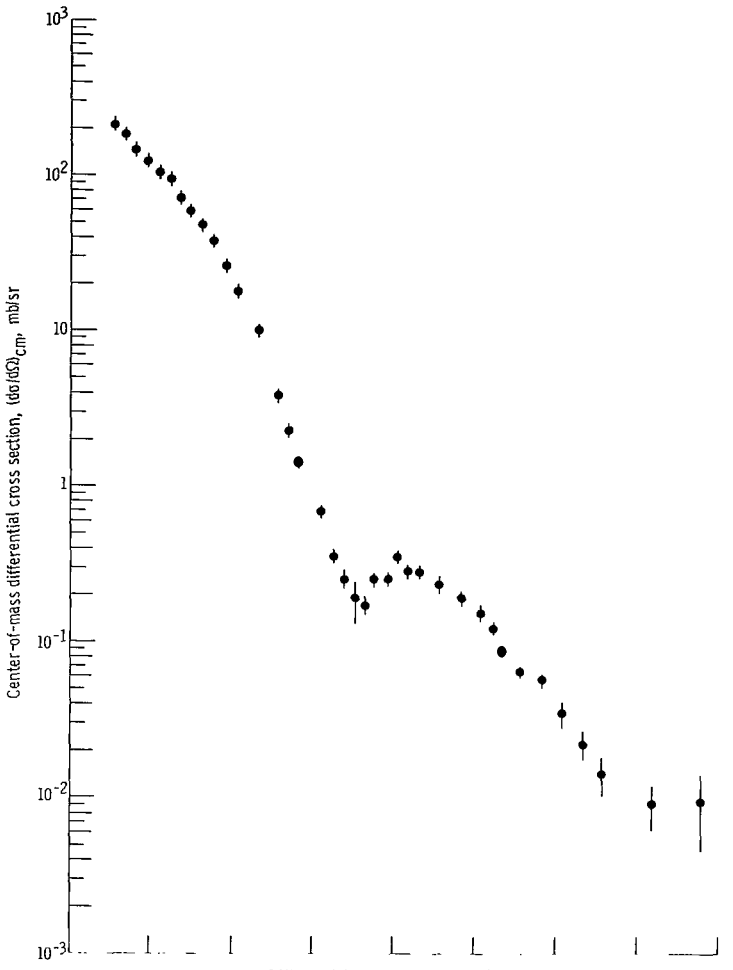

(a) Differential cross section, at 587 MeV.

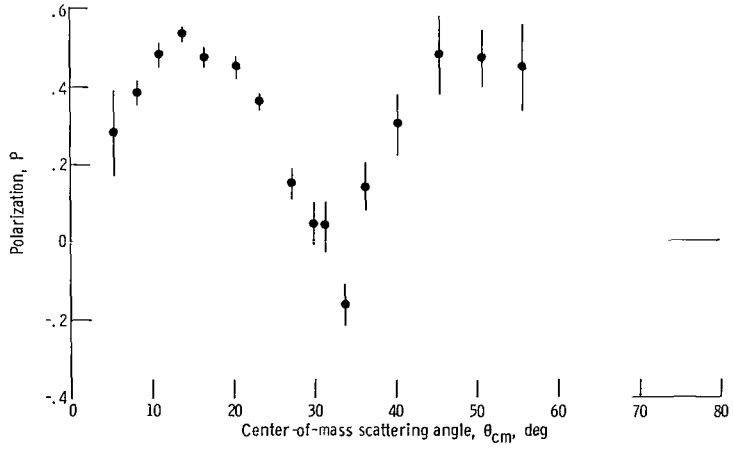

(b) Polarization, at 544 MeV.

Figure 16. - p-^{4}He differential cross section and polarization as function of center-of-mass scattering angle.

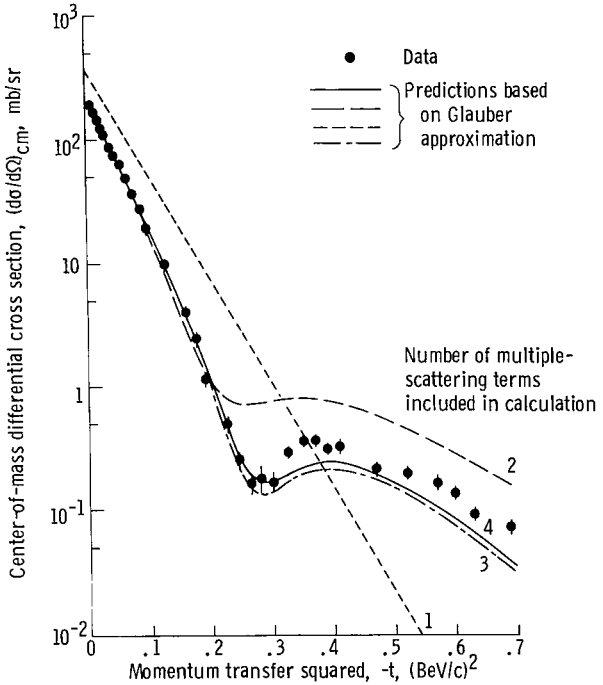

Figure 17. - Comparison of p-^{4}He data with calculations based on the Glauber approximation, for 587 MeV. Nuclear radius, R = 1.25 fermi; slope of nucleon-nucleon cross section, a = 4.3 $(GeV/c)^{-2}$; ratio of real to imaginary part of nucleon-nucleon scattering amplitude, $\alpha_P = \alpha_n = -0.43$; total nucleon-nucleon cross section, $\sigma_P = \sigma_n = 3.9$ fermi squared.

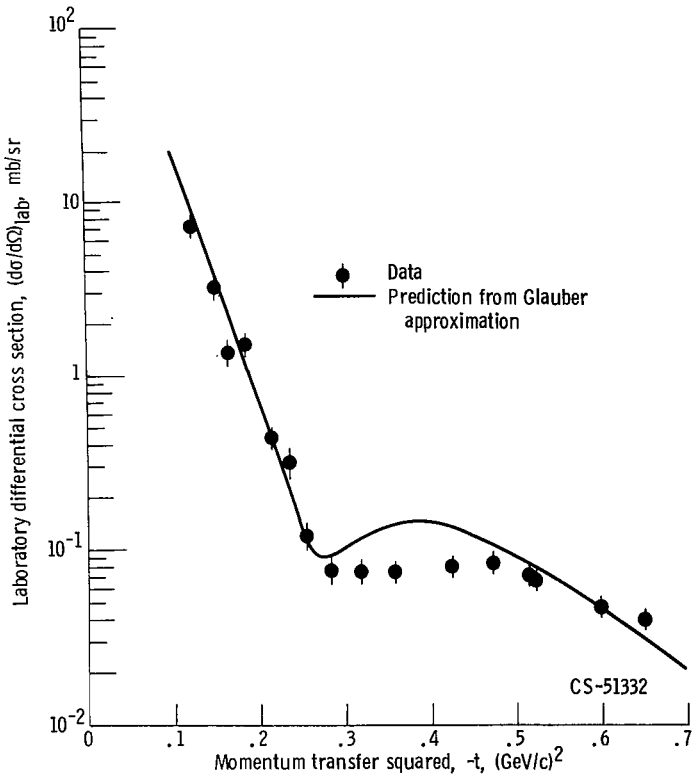

Figure 18. - Comparison of p-^{3}He data with calculation based on the Glauber approximation, for 582 MeV.

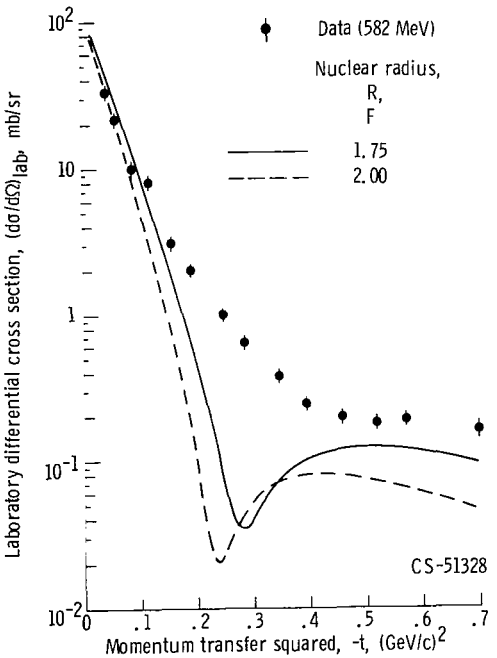

Figure 19. - Comparison of p-D data with calculations based on the Glauber approximation using two different radii in the Gaussian wave function.

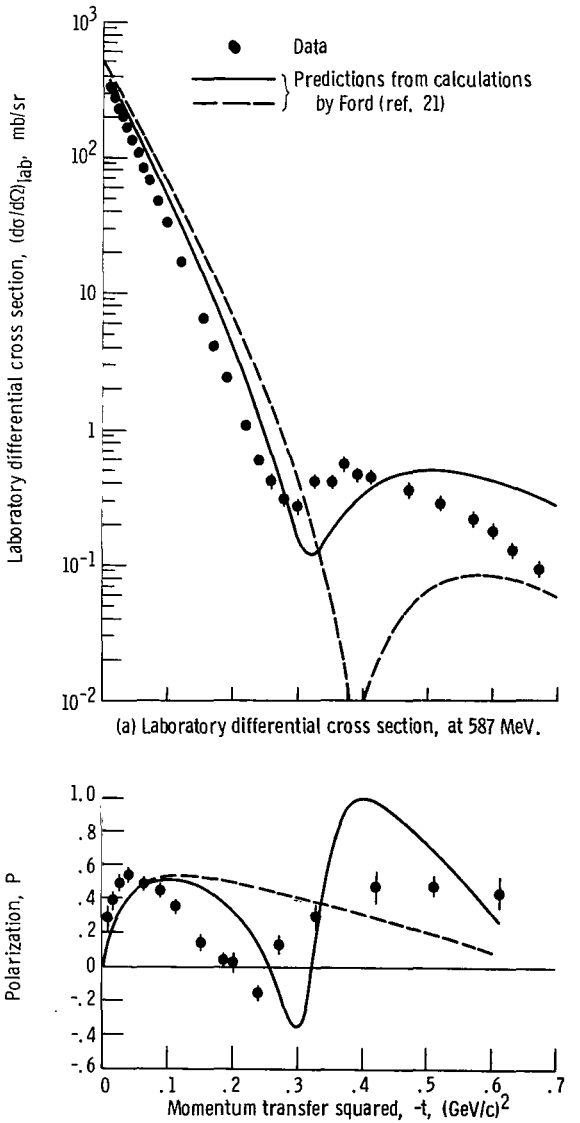

Figure 20. - Comparison of p-^{4}He cross section and polarization with predictions based on calculations by Ford.

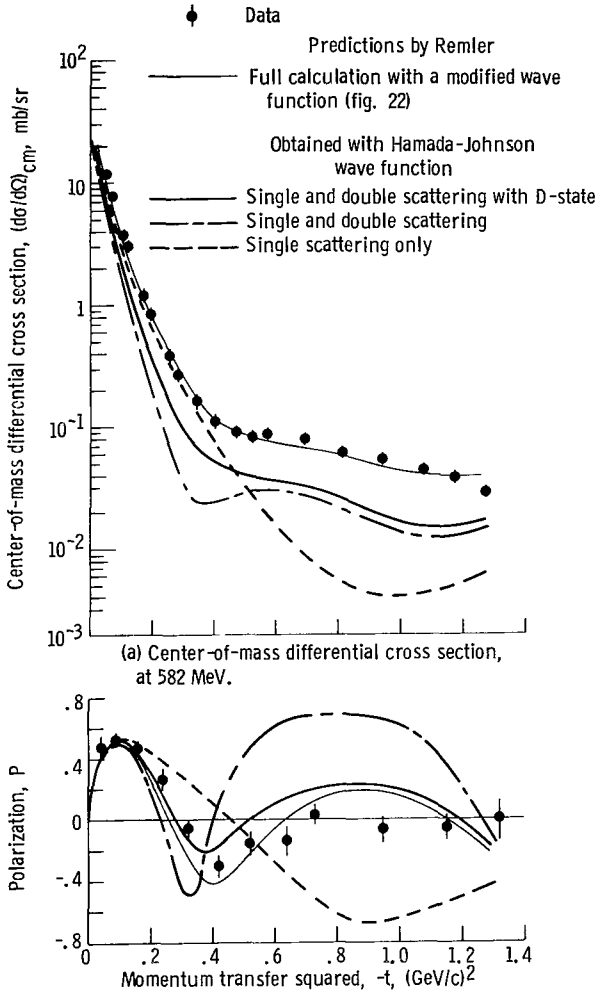

(a) Center-of-mass differential cross section, at 582 MeV.

(b) Polarization, at 544 MeV.

Figure 21. - Comparison of p-D differential cross section and polarization with calculations by Remler (ref. 31).

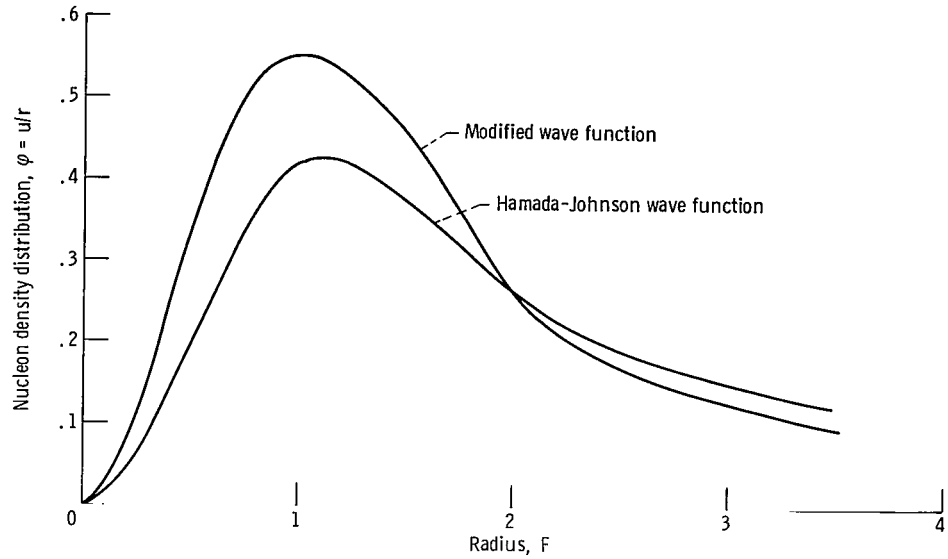

Figure 22. - Comparison of wave function obtained by Remler in search to fit p-D data with the Hamada-Johnson wave function.

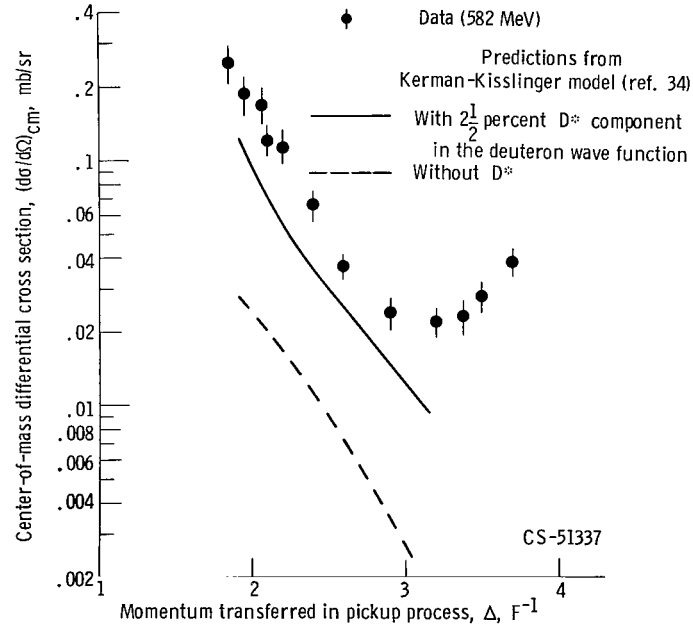

Figure 23. - Large-angle p-D cross section from present experiment plotted as function of momentum transferred in pickup reaction.

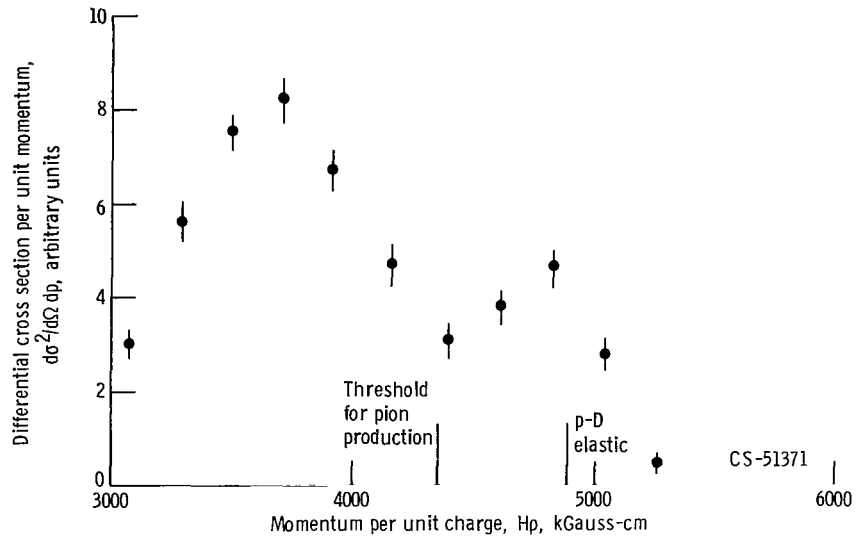

Figure 24. - Momentum distribution of high-energy deuterons knocked out of beryllium-9. Deuteron angle, 12°.

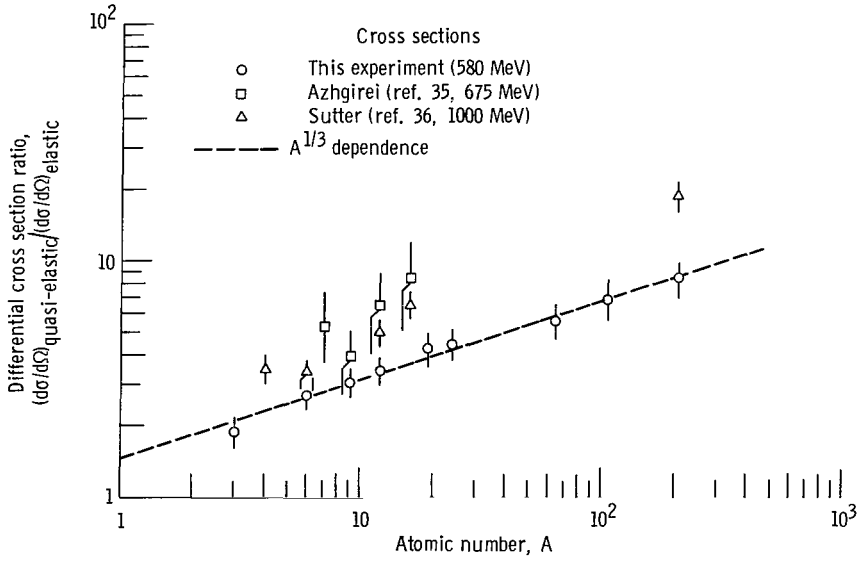

Figure 25. - Cross sections for quasi-free p-D scattering in various nuclei.

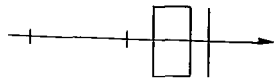

(a) True coincident event.

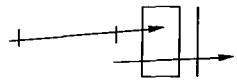

(b-1)

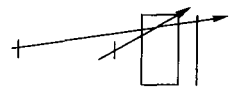

(b-2)

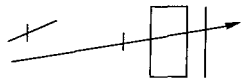

(b-3)

(b) Coincident event composed of a true coincident event in two detectors and a random event in the third detector.

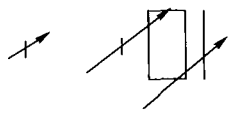

(c) Completely random event.

Figure 26. - Possible first-order coincidence in a three-detector telescope with an absorber between detectors 2 and 3.

"The aeronautical and space activities of the United States shall be conducted so as to contribute . . . to the expansion of human knowledge of phenomena in the atmosphere and space. The Administration shall provide for the widest practicable and appropriate dissemination of information concerning its activities and the results thereof."

—NATIONAL AERONAUTICS AND SPACE ACT OF 1958

NASA SCIENTIFIC AND TECHNICAL PUBLICATIONS

TECHNICAL REPORTS: Scientific and technical information considered important, complete, and a lasting contribution to existing knowledge.

TECHNICAL NOTES: Information less broad in scope but nevertheless of importance as a contribution to existing knowledge.

TECHNICAL MEMORANDUMS: Information receiving limited distribution because of preliminary data, security classification, or other reasons.

CONTRACTOR REPORTS: Scientific and technical information generated under a NASA contract or grant and considered an important contribution to existing knowledge.

TECHNICAL TRANSLATIONS: Information published in a foreign language considered to merit NASA distribution in English.

SPECIAL PUBLICATIONS: Information derived from or of value to NASA activities. Publications include conference proceedings, monographs, data compilations, handbooks, sourcebooks, and special bibliographies.

TECHNOLOGY UTILIZATION PUBLICATIONS: Information on technology used by NASA that may be of particular interest in commercial and other non-aerospace applications. Publications include Tech Briefs, Technology Utilization Reports and Notes, and Technology Surveys.

Details on the availability of these publications may be obtained from:

SCIENTIFIC AND TECHNICAL INFORMATION DIVISION

NATIONAL AERONAUTICS AND SPACE ADMINISTRATION

Washington, D.C. 20546